

An image-based array trigger for Imaging Atmospheric Cherenkov Telescope Arrays

Hugh Dickinson^{a,b,*}, Frank Krennrich^a, Amanda Weinstein^a, Jonathan Eisch^a, Karen Byrum^c, John Anderson^c, Gary Drake^c

^a*Department of Physics & Astronomy, Iowa State University, Zaffarano Hall, 2334 Pammel Drive, Ames, IA 50011-3160, United States of America*

^b*School of Physics and Astronomy, 275-04 Tate Laboratory of Physics, 116 Church St. SE, Minneapolis, MN 55455, United States of America*

^c*High Energy Physics Division, 9700 S. Cass Avenue, Building 362, Argonne, IL 60439, United States of America*

Abstract

It is anticipated that forthcoming, next generation, atmospheric Cherenkov telescope arrays will include a number of medium-sized telescopes that are constructed using a dual-mirror Schwarzschild-Couder configuration. These telescopes will sample a wide (8°) field of view using a densely pixelated camera comprising over 10^4 individual readout channels. A readout frequency congruent with the expected single-telescope trigger rates would result in substantial data rates. To ameliorate these data rates, a novel, hardware-level Distributed Intelligent Array Trigger (DIAT) is envisioned. A copy of the DIAT operates autonomously at each telescope and uses reduced resolution imaging data from a limited subset of nearby telescopes to veto events prior to camera readout and any subsequent network transmission of camera data that is required for centralized storage or aggregation. We present the results of Monte-Carlo simulations that evaluate the efficacy of a “Parallax width” discriminator that can be used by the DIAT to efficiently distinguish between genuine gamma-ray initiated events and unwanted background events that are initiated by hadronic cosmic rays.

Keywords: Gamma-Ray Astronomy, Array Trigger, Gamma-Hadron Separation, Advanced Algorithm, Energy Threshold Reduction

1. Introduction

Gamma-ray astronomy with ground-based instruments was enabled by the pioneering efforts by the Whipple collaboration (Weekes et al., 1989) by demonstrating the excellent inherent sensitivity of imaging atmospheric Cherenkov telescopes (IACTs) for detecting astrophysical TeV photons.

The detection of several astrophysical sources (the Crab Nebula and several blazars including Mrk 421, Mrk 501, 1ES 2344+524, H 1426+428, 1ES 1959+650) with the Whipple 10 m, HEGRA and CAT instruments in the mid-1990s motivated construction of the current generation of telescopes (H.E.S.S. (Aharonian et al., 2006), MAGIC-II (Aleksić et al., 2012) and VERITAS (Holder et al., 2006)) in the early twenty first century. These modern instruments employ the stereoscopic imaging technique and exceed the sensitivity of any previous TeV gamma-ray telescope by an order of magnitude. The future potential of TeV astronomy to explore high energy astrophysics and

particle astrophysics is amply demonstrated by a collective catalog of over two hundred TeV γ -ray sources¹.

Observations of celestial photons with energies in the interval 20 GeV - 300 TeV address important questions of modern astrophysics and particle physics. Indeed, γ -ray astronomy promises key insights for a diverse range of topics including: the origin of cosmic rays; particle acceleration and propagation; cosmological radiation and magnetic fields and even the composition and nature of dark matter (see e.g. Acharya et al., 2013). Future IACTs will also provide important follow-up observations of sources that are identified at energies above 0.1 GeV by the *Fermi* space telescope’s all-sky survey. To date, *Fermi* has delivered a catalog containing over 3000 distinct γ -ray sources (Acero et al., 2015), of which only a small fraction have been studied at multi-TeV energies. The forthcoming Cherenkov Telescope Array (CTA; Acharya et al., 2013) will extend the energy coverage of the *Fermi* survey to span six orders of magnitude in energy, with sufficient sensitivity to perform statistically rich population studies for source classes in the 100 TeV regime. CTA will exhibit substantially improved angular resolution and reduced background contamination with respect to current-generation instruments. These enhancements are expected to permit the establishment of multiwavelength associations for over 1000 sources

*Corresponding author

Email addresses: hdickins@umn.edu, hughd@iastate.edu (Hugh Dickinson), krennrich@iastate.edu (Frank Krennrich), amandajw@iastate.edu (Amanda Weinstein), jeisch@iastate.edu (Jonathan Eisch), byrum@anl.gov (Karen Byrum), jta@anl.gov (John Anderson), jta@anl.gov (Gary Drake)

¹TeVCat: <http://tevcat.uchicago.edu>

that were discovered by Fermi but lack a plausible counterpart at other wavelengths.

Building on the nascent successes of this new research field, the CTA project has been undertaken by a worldwide collaboration of scientists who have coalesced around the shared goal of constructing and operating a next-generation IACT array. The basic concept of CTA (see e.g. Acharya et al., 2013) envisions heterogeneous arrays comprising telescopes with differing sizes and capabilities. The prevalent designs include a large number of small-sized telescopes (SSTs, $\varnothing_{\text{mirror}} \sim 4$ m), several tens of medium-size telescopes (MSTs, $\varnothing_{\text{mirror}} \sim 10 - 12$ m) and a small number of large-size telescopes (LSTs, $\varnothing_{\text{mirror}} \sim 23$ m), which combine to provide wide energy coverage spanning 20 GeV - 100 TeV.

The MSTs probe the sub-TeV to multi-TeV energy band, which is a regime for which the IACT technique achieves maximal sensitivity and excellent angular resolution. At higher energies, the Cherenkov light intensity for γ -ray showers is substantially increased, such that detection and imaging becomes feasible using smaller mirror areas provided by SSTs. Conversely, large mirror areas provided by the LSTs are required in order to access the 20 - 100 GeV regime, for which the Cherenkov light intensity is faint.

The energy ranges to which each telescope type is sensitive exhibit substantial overlap but the effective collection areas (see e.g. Acharya et al., 2013) for sub-arrays comprising the MSTs and LSTs are markedly disparate ($\sim 1\text{km}^2$ and $\sim 0.1\text{km}^2$, respectively). A substantial increase in low-energy event statistics could be achieved by enabling detection of $\lesssim 100$ GeV γ -rays using the MST sub-array, thereby augmenting the much smaller effective collection area of the LSTs in this energy regime. Accordingly, it is important to consider how improvements in their electronics designs could enhance the low energy response of MSTs.

Compelling scientific motivation for improving the sensitivity in the sub-100 GeV regime is provided by a renewed interest in γ -ray emission from pulsars, especially examples that exhibit an unexpected emission component in the 10 - 100 GeV regime. A further motivation is the potential to expand the size of the observable Universe for IACTs. On cosmological distance scales, the extragalactic background light strongly attenuates photons with energies exceeding ~ 10 s of GeV according to an opacity that increases with γ -ray energy (e.g. Dwek and Krennrich, 2013).

In this paper we describe a *Decentralized Intelligent Array Trigger* (DIAT) system that is specifically designed to enable operation of IACTs with a low energy threshold, while maintaining stable and manageable data rates in the presence of varying observing conditions and ambient illumination. Transient brightening of the night sky background light (NSB) can occur for several reasons including partial cloud coverage during moonless nights, observing the bright regions in the galactic plane or observation with

partial moonlight. Stable telescope operation across these regimes would require the adjustment of the *single telescope* trigger threshold, if the rates were not moderated by a hardware *array* trigger. Telescope and array triggering strategies are discussed further in §2.

In addition to mitigating the effect of bright NSB, the DIAT system we present is also capable of substantially reducing the background trigger rate produced by cosmic-ray-induced air showers. Configurable firmware can selectively tune the background rate suppression from factors of a few up to two orders of magnitude, while maintaining an acceptably high acceptance for gamma-ray events.

The capabilities of the DIAT system are particularly well suited for a highly innovative telescope design (e.g. Vassiliev and Fegan, 2008), which uses a dual-mirror *Schwarzschild Couder* (SC) configuration, and incorporates a finely pixelated camera comprising 11,328 independent silicon photomultiplier-based readout channels (Otte et al., 2015).

This SC telescope (SCT) design provides a wide field of view ($\sim 8^\circ$) and high-resolution imaging of air showers with excellent angular and energy resolution. However, the large number of pixels combined with a nominal camera trigger rate of 10 kHz per telescope implies a substantial cost in terms of data transfer, storage and processing requirements. Reduction in overall data volume can be achieved at the trigger level using front-end electronics and potentially further by off-line post-processing.

2. Telescope and Array-Level Triggering

IACTs operate in a strongly background-dominated regime. *Array* triggering schemes use information from multiple telescopes to veto many background events *before* camera readout, with the goal of stabilizing the array's energy threshold and dead time under variable ambient illumination. For the densely pixelated SCT camera, control over the array trigger rate is also desirable to guarantee that data-transfer rates remain tractable at the extremes of normal observing conditions.

The overwhelming majority of individual *pixel* triggers are associated with low-level illumination from the ambient night-sky background light. The NSB induces a rate of random pixel triggers that is often sufficient to generate a large rate of spurious individual *telescope* triggers.

To address this issue, current-generation IACTs implement *multi-level* hardware trigger systems that require sequential fulfillment of criteria that involve signals from an increasing number of imaging elements (See e.g. Funk et al., 2004; Moudou et al., 2011; Weinstein, 2008; Zitzer, 2013; Paoletti et al., 2007; López-Coto et al., 2016, for more details regarding the trigger systems of H.E.S.S., MAGIC-II and VERITAS). Triggering of a single *telescope* typically requires a cluster of adjacent camera pixels to trigger within a temporal coincidence window lasting a few nanoseconds. This precaution substantially reduces the rate of telescope triggers caused by the accidental pileup of night sky background photons in a single pixel.

For typical sky brightnesses, the intensity of NSB photons is such that the rate of NSB-induced triggers becomes negligible for per-pixel signals exceeding ~ 5 photons. For larger per-pixel photon intensities, another background component comprising *temporally correlated* Cherenkov light from cosmic-ray (CR) initiated air showers becomes dominant. Modern multi-telescope IACT arrays reduce contamination from CRs using some variant of a *multiplicity* trigger that requires a minimum of two telescopes to trigger within 50 - 100 ns. Basic multiplicity array trigger systems help to stabilize the data rates at which these telescopes must operate, primarily by rejecting a faint subset of cosmic-ray- and single-muon-induced showers that trigger only a single telescope. CR-initiated air-showers that trigger multiple telescopes often exhibit temporal correlation between individual telescope triggers that is sufficient to impair the efficacy of traditional multiplicity array triggers.

The DIAT concept represents a significant extension to the functionality of existing array trigger schemes. It is the first system to use imaging information to discriminate between γ -ray- and cosmic-ray-induced shower images in real time at the *hardware trigger* level. This has become possible thanks to the recent emergence of fast Field Programmable Gate Arrays (FPGAs) that can evaluate and apply individual camera trigger criteria while simultaneously performing reduction of the camera pixel hit pattern into summary image parameters in real-time. Rapid computation using the image parameters that are generated by neighbouring telescopes within the array permits near-real-time stereo analysis of the event.

Subsequent sections demonstrate that spurious CR-induced triggers *can* be identified and vetoed in near-real-time by processing reduced image data using modern FPGAs. In section 3 we define the *parallax width* event discriminator and mathematically describe the algorithm that is used to compute it. Section 4 outlines how excessive trigger suppression for high energy γ -ray events can be ameliorated by indiscriminately accepting events that surpass a combined image brightness threshold. In section 5, we provide a brief description of a distributed hardware array trigger that could be used to deployed to compute the *parallax width* in near real-time for large IACT arrays. Section 6 presents and examines our results, which were obtained by applying the *parallax width* algorithm to discriminate between simulated γ -ray- and proton-like events for a variety of γ -ray source configurations. We summarize our results in section 7. Overall, we explicitly show that image parameters involving only the first moments of each telescope image are sufficient to discriminate between hadronic and γ -ray-induced showers. If the rate of spurious telescope triggers can be effectively controlled, then the sensitivity of an IACT array to low energy γ -rays can be enhanced by reducing the trigger threshold of individual camera pixels.

We note that there exist alternative proposals for data rate suppression that do not use multi-telescope informa-

tion, and do not veto events in their entirety. Instead, such schemes implement strategies for lossy compression of event data by discarding segments of the Cherenkov image that are signal-free or deemed unlikely to contain signals produced by Cherenkov light (e.g. Contreras et al., 2015; Naumann et al., 2013; López-Coto et al., 2016).

3. The Parallax Width Discriminator

Electromagnetic air-showers initiated by γ -rays are characterized by a single shower axis, and triggered telescopes capture coherent elliptical images with a well defined nucleus-within-coma structure. In contrast, the hadronic component of cosmic-ray showers produces multiple sub-showers and typically yields a more fragmentary distribution of Cherenkov light (see e.g. Fegan, 1997). The *parallax width* (Krennrich and Lamb, 1995; Krennrich et al., 2008; Schroedter et al., 2009) discriminator (P) leverages the difference between CR and γ -ray shower images to rapidly distinguish between these event categories at the *hardware* level. It is instructive to separate the distinct algorithmic stages that comprise the computation of P into two separate categories: Camera Image Preprocessing, and Computation of the Parallax Width Discriminator which are described in §3.2 and §3.3, respectively.

3.1. Telescope Simulation Framework

To investigate the efficacy of P to distinguish γ -ray and cosmic-ray initiated air-showers, simulations of the SCT array configuration were produced using the `sim_telarray` software package (Bernlöhr, 2008). Simulations of γ -ray emission from point-like and diffuse ² sources, as well as simulations of a diffuse proton background were used. The energy spectra of the simulated γ -rays and protons described falling power-law distributions ($dN/dE \propto E^{-\Gamma_x}$: $x \in \{\gamma, p\}$) with spectral indices $\Gamma_\gamma = 2$ and $\Gamma_p = 2.7$, respectively³. Unless it is stated otherwise, γ -ray events model astrophysical sources located centrally in the field of view at an altitude of 70° and an azimuth of 180° . The raw simulated camera images were provided as input to a computer simulation of the DIAT array triggering scheme.

3.2. Camera Image Preprocessing

Before P is computed, preprocessing algorithms are applied to each camera image at the single telescope level. Figure 1 illustrates the manner in which telescope-specific camera data are processed to derive a compact geometrical representation of the captured shower image.

² γ -ray events were simulated with randomly distributed arrival directions, distributed within a cone with a 10° opening angle around the telescope pointing axis. Such an event distribution appears genuinely diffuse for the SCT, which has an 8 degree field of view.

³Although γ -ray spectra with indices as hard as 2 are seldom observed in nature, using simulated events with $\Gamma_\gamma = 2$ enables the performance of the parallax width trigger to be evaluated with good number statistics for high γ -ray energies.

To mitigate the effect of Night Sky Background photons randomly triggering each of the 11,328 individual readout channels, and thereby enable a reduction of the trigger threshold, 2,832 lower resolution *super-pixels*⁴ are formed from four adjacent imaging pixels. The combined signal amplitudes of the super-pixels are used to form a Boolean-valued *trigger image* with a predefined threshold on the summed output level (n_{pe} , typically expressed in photoelectron-equivalent units, hereafter *p.e.*) segregating true (triggered) and false values. An *individual telescope* is deemed to have triggered if its Boolean trigger image includes 3 or more adjacent triggered super-pixels⁵.

A two-level image cleaning algorithm is applied to each trigger image to remove small clusters of NSB-induced pixel triggers that can incorrectly trigger the telescope or bias subsequent computation of P by contaminating valid telescope images with noise. Nominally triggered pixels are retained in the cleaned trigger image if valid triggers were generated by *at least* n_1 immediately adjacent pixels, *at least one* of which *itself* has n_2 triggered neighbours⁶. This cleaning algorithm is designed to retain extended contiguous groups of trigger pixels that are consistent with genuine air-shower images. Figures 2 and 3 demonstrate the algorithm for an image of a γ -ray-initiated air shower event and an image that contains a large number of randomly triggered super-pixels, respectively. Most triggered pixels in the genuine γ -ray event are retained, while the sparse pixels that are randomly triggered are removed.

3.3. Computation of the Parallax Width Discriminator

Table 1 summarizes the notation used in the subsequent derivation which also uses the index variable i to enumerate the set of all triggered telescopes.

1. For each telescope that triggers, the *centroid*-vector $\mathbf{r}_{C,i}$ of the coarsely-sampled trigger image is defined as the mean camera-coordinates of the set of triggered super-pixels.
2. For each centroid vector, a second vector $\mathbf{r}_{F,i} = \mathbf{r}_{C,i} - \mathbf{r}^*$ is defined where \mathbf{r}^* is an arbitrarily selected *fiducial* camera-plane coordinate $\mathbf{r}^* = (x_C^*, y_C^*)$.⁷ For real telescope arrays, the introduction of \mathbf{r}^* provides the flexibility to correct for non-uniform mechanical deformations of individual telescope structures, or non-parallel telescope pointing modes, and ensure that $\mathbf{r}_{F,i}$ corresponds to the projection of identical celestial coordinates in all telescope cameras. This

⁴Throughout this work the terms *super-pixel* and *trigger pixel* are considered to be synonymous and are used interchangeably.

⁵Super-pixels are considered to be adjacent if they share at least one common vertex.

⁶The multilevel neighbour multiplicities for the cleaning algorithm were fixed to $n_1 = 3$ and $n_2 = 5$ after empirical investigation indicated good performance using these values.

⁷The *direction* of this vector is hereafter described as the *forward* direction and intersections between pairs of vectors along their forward directions are described as *forward intersections*.

study simulates all telescopes identically and computation of P is simplified by defining \mathbf{r}^* to be the camera centre $(0, 0)$.

The events shown in each panel of Figures 4 and 5 provide representative examples of γ -ray and proton-initiated events with various simulated characteristics. They illustrate how the subsequent algorithmic operations are used to compute P for each event class.

1. The direction of each computed \mathbf{r}_F^* vector is projected from the independent coordinate systems of each telescope camera plane into a unified coordinate system spanning the *mirror plane* of the telescope array, defining a set of *projected* vectors $\{\mathbf{r}'_{F,i}\}$. The mirror plane is defined to intersect the mean of the geographical coordinates of all telescopes comprising the complete array and to lie perpendicular to their common pointing axes.⁸
2. A set of n_\times mirror-plane coordinates $\{\mathbf{r}'_{\times,j}\}$ is computed that corresponds to the *forward* intersections between the projected $\{\mathbf{r}'_{F,i}\}$ vectors. Only intersections that subtend angles $20^\circ < \theta_\times < 160^\circ$ are used for the computation of P .⁹ The index variable j is used to enumerate the set of all forward intersections.
3. Finally, the *parallax width* is defined as the dispersion of the intersection coordinates

$$P = \sqrt{\frac{\sum_j |\mathbf{r}'_{\times,j} - \langle \mathbf{r}'_{\times,j} \rangle|^2}{n_\times}}. \quad (1)$$

The *upper*, *lower* panels of Figure 4 and the *upper* panel of Figure 5 all correspond to γ -ray-initiated events. For such events, the computed trigger-image centroids $\mathbf{r}_{C,i}$ correspond closely with the camera-plane projection of a single point in 3-dimensional space. This point lies close to the air-shower axis at the height of maximal Cherenkov emission. The fiducial camera coordinate $\mathbf{r}^* = (0, 0)$ is also the camera-plane projection of a second, infinitely distant point that is identical for all telescopes. For γ -ray-initiated events, each $\mathbf{r}_{F,i}$ connects projected points that are effectively identical for all telescopes. Accordingly, the mapping $\{\mathbf{r}_{F,i}\} \rightarrow \{\mathbf{r}'_{F,i}\}$ yields a set of vectors which intersect at a tightly clustered region of the array mirror plane and the computed value of P is small.

Figure 4 (*top*) corresponds to a γ -ray-initiated event aligned with the telescopes' optical axes (*on-axis*). The arrival directions of on-axis events correspond precisely with the fiducial camera-plane coordinate $\mathbf{r}^* = (0, 0)$, when pro-

⁸Accordingly, *if* the telescopes of the array were coaligned to point vertically upwards, then the mirror plane and ground plane would be identical.

⁹Intersections that subtend angles outside of this range are excluded since discretization of the camera image induces small errors affecting the computation of the $\{\mathbf{r}'_{F,i}\}$ which can amplify to produce large, spurious offsets when the $\{\mathbf{r}'_{\times,j}\}$ are computed.

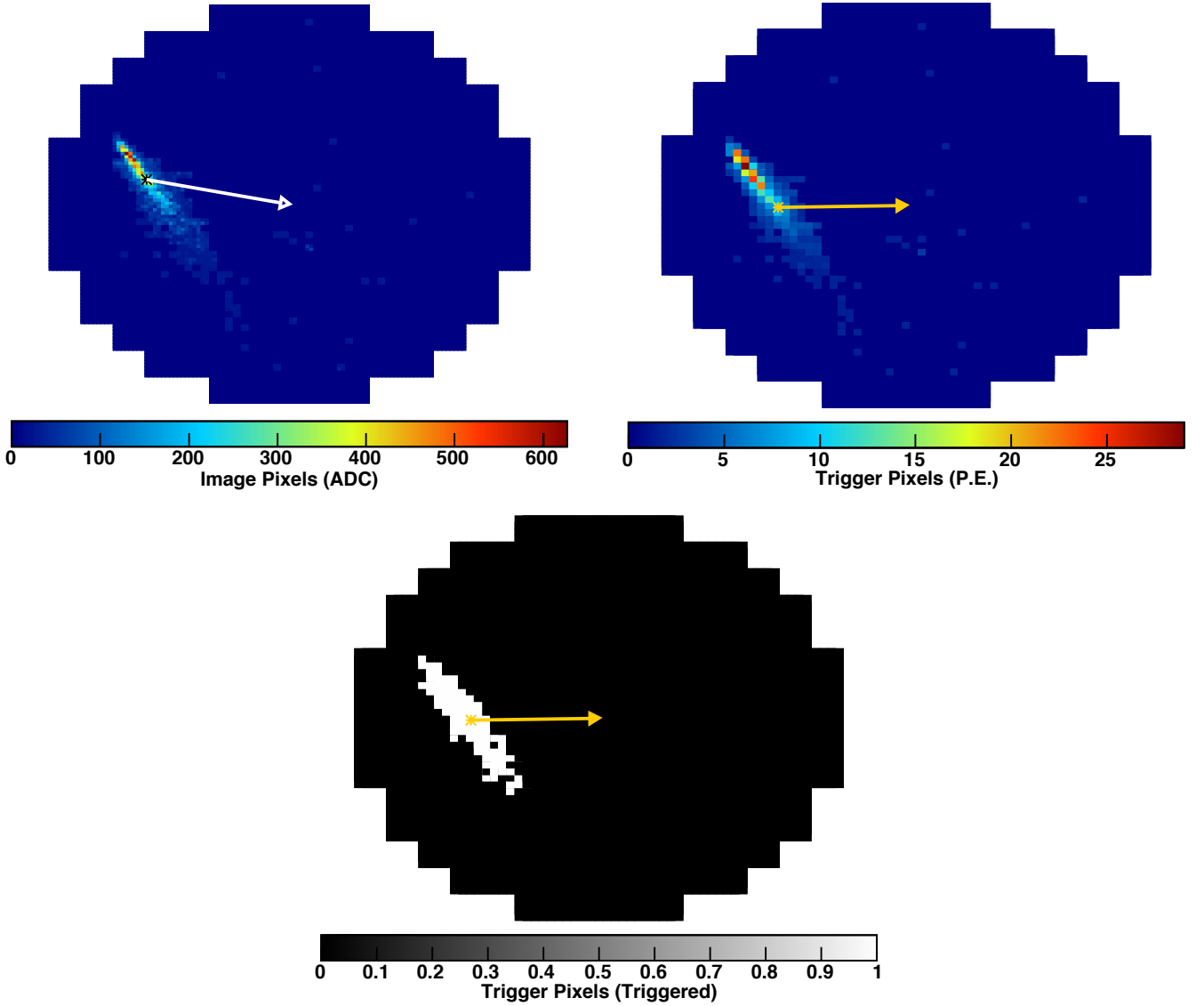


Figure 1: The *upper-left-hand* panel illustrates an unprocessed, finely pixelated image corresponding to a γ -ray-initiated air-shower. The *upper-right-hand* panel illustrates the intermediate, coarsely pixelated image that is derived by combining the signals from sets of 4 neighbouring imaging pixels. The *lower* panel illustrates the Boolean-valued trigger image that is required by the algorithm that computes P . The *orange* arrows correspond to the vector \mathbf{r}_F , which connects the implicitly *unweighted* trigger-image centroid with the *fiducial* camera-plane coordinate $\mathbf{r}^* = (0, 0)$ at the camera centre. For comparison, the *white* arrow (*top-left-hand* panel) connects the *signal-amplitude-weighted* mean position of all *imaging* pixels with \mathbf{r}^* .

Coordinate System	Symbol	Description
Camera Plane	$\mathbf{r}_{C,i}$	The coordinates of the centroid of the boolean-valued <i>trigger image</i> for the i th telescope.
	$\mathbf{r}_{F,i}^*$	The vector pointing from the centroid of the boolean-valued <i>trigger image</i> to the camera centre for the i th telescope.
Mirror Plane	$\mathbf{r}'_{F,i}$	The projection of $\mathbf{r}_{F,i}^*$ from the camera plane into the array mirror plane for each telescope.
	$\mathbf{r}'_{\times,j}$	The mirror plane coordinates of a forward intersection between the $\mathbf{r}'_{F,i}$ for two separate telescopes.

Table 1: Notation used in the derivation of P .

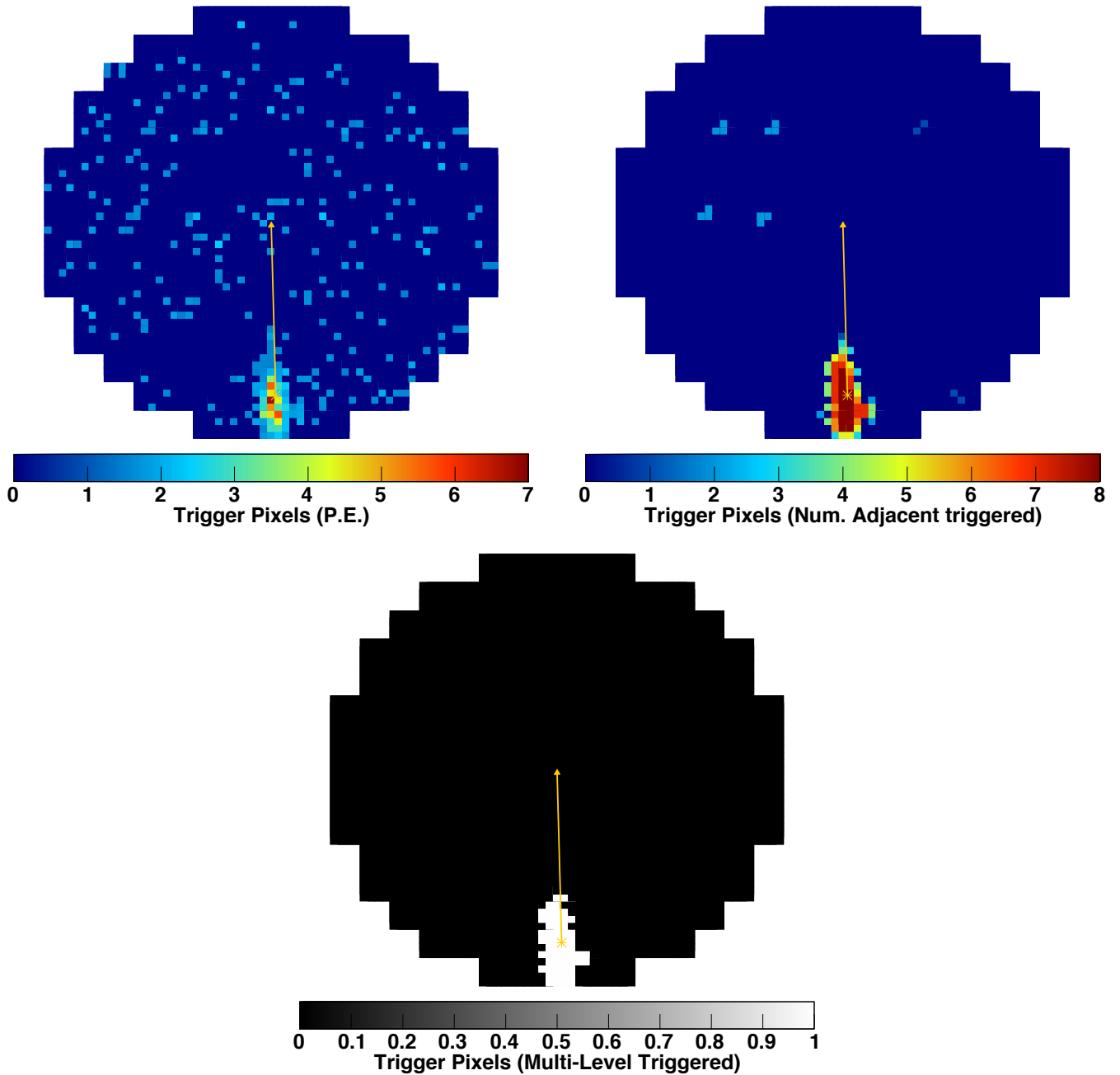


Figure 2: Demonstration of the two-level cleaning algorithm for $n_1 = 3$, $n_2 = 5$ and a pixel threshold $n_{pe} = 2$ p.e. when applied to a genuine γ -ray image. The *upper-left* panel shows signals registered by each triggered superpixel in photoelectron equivalent counts. The number of triggered neighbours for each super-pixel is illustrated in the *upper-right* panel. The *lower* panel reveals the result of applying the two-level cleaning algorithm to the original trigger image.

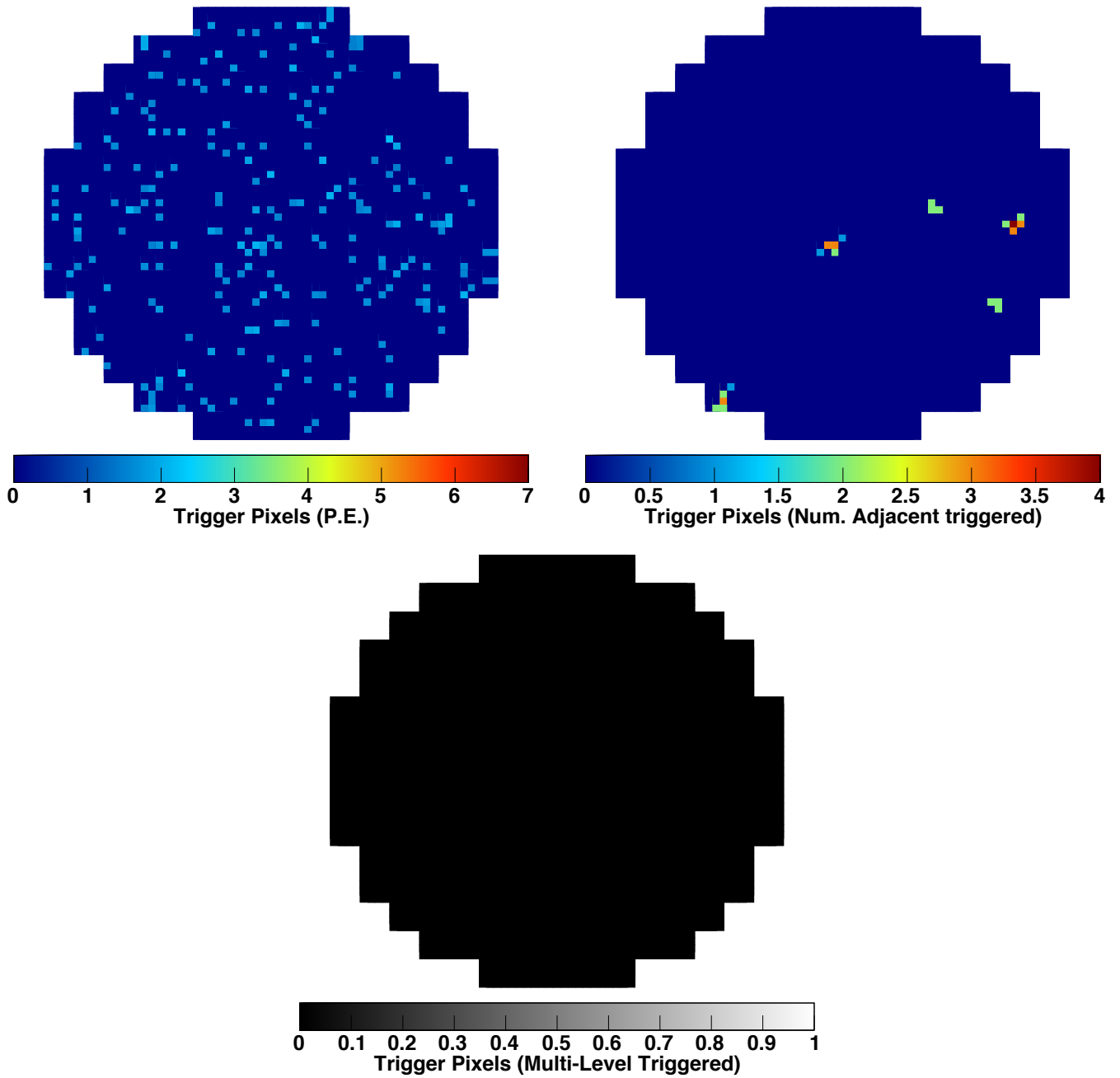


Figure 3: Demonstration of the two-level cleaning algorithm for $n_1 = 3$, $n_2 = 5$ and a pixel threshold $n_{pe} = 2$ p.e. when applied to an image comprising randomly triggered super-pixels that would otherwise be sufficiently numerous to fulfill the pass-through criterion ($n_{TP} > 16$). The panels correspond to their counterparts in Figure 2.

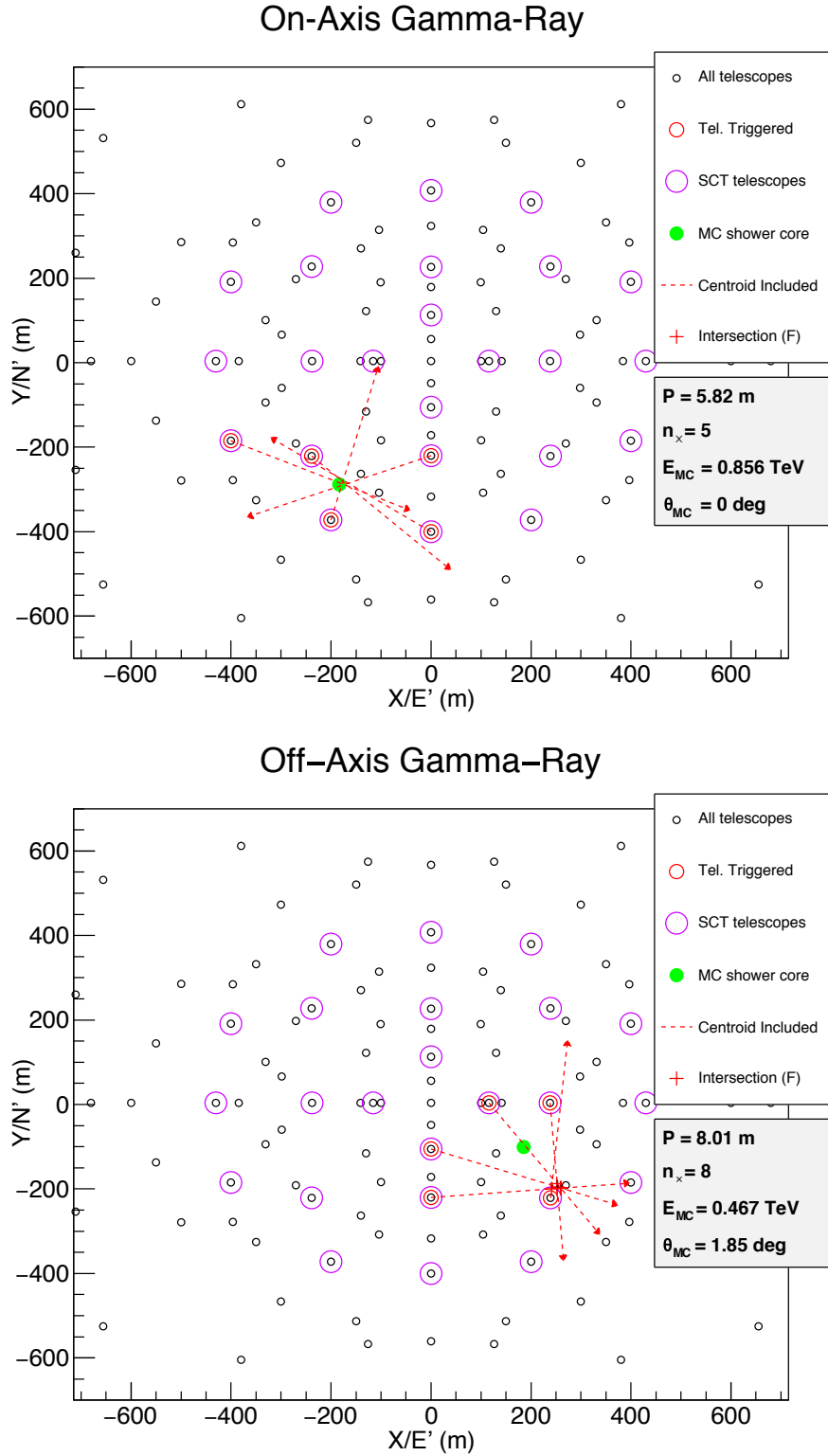
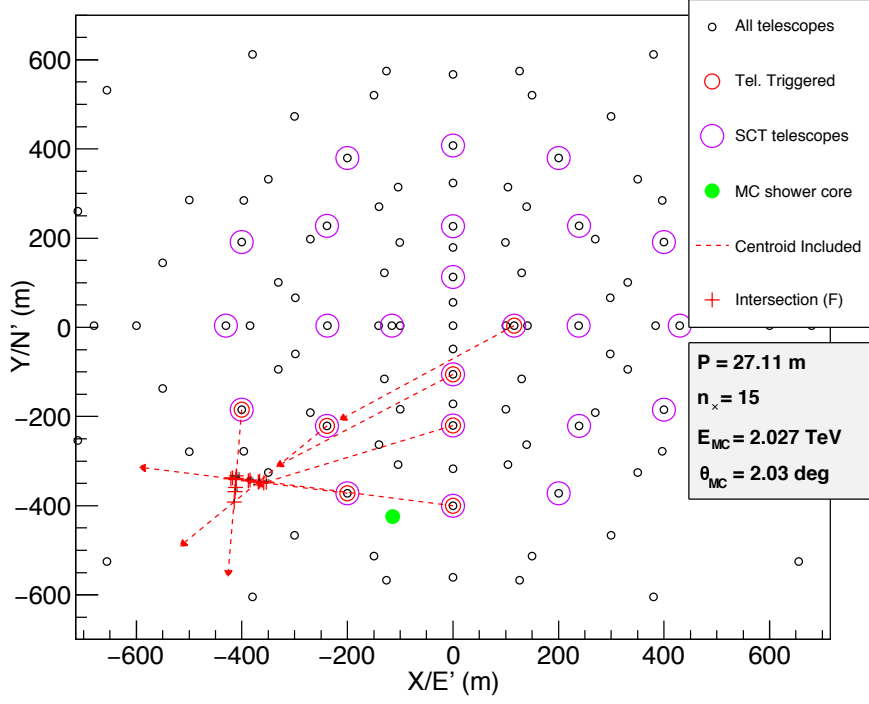


Figure 4: Array mirror plane projections illustrating P computation for an on-axis γ -ray event (*top*), and an off-axis γ -ray event with $E_\gamma \lesssim 2 \text{ TeV}$ (*bottom*). Red circles identify SCT telescopes (magenta circles) that triggered. Red dashed arrows indicate the projected direction of $\mathbf{r}'_{F,i}$ for each telescope in the array that generated a valid trigger-image. Red crosses are used to indicate the set of valid *forward* intersections $\{\mathbf{r}'_{x,j}\}$ between the $\{\mathbf{r}'_{F,i}\}$. The green marker indicates the coordinates at which the shower core intersects the mirror plane. Grey panels list the computed values of P , the number of *forward* intersections for which $20^\circ < \theta_x < 160^\circ$ (n_x) that were used in the computation, the *true* energy (E_{MC}) of the simulated event, and the *true* angular offset (θ_{MC}) of the between the incident particle direction and the array pointing.

High Energy Off-Axis Gamma-Ray



Proton

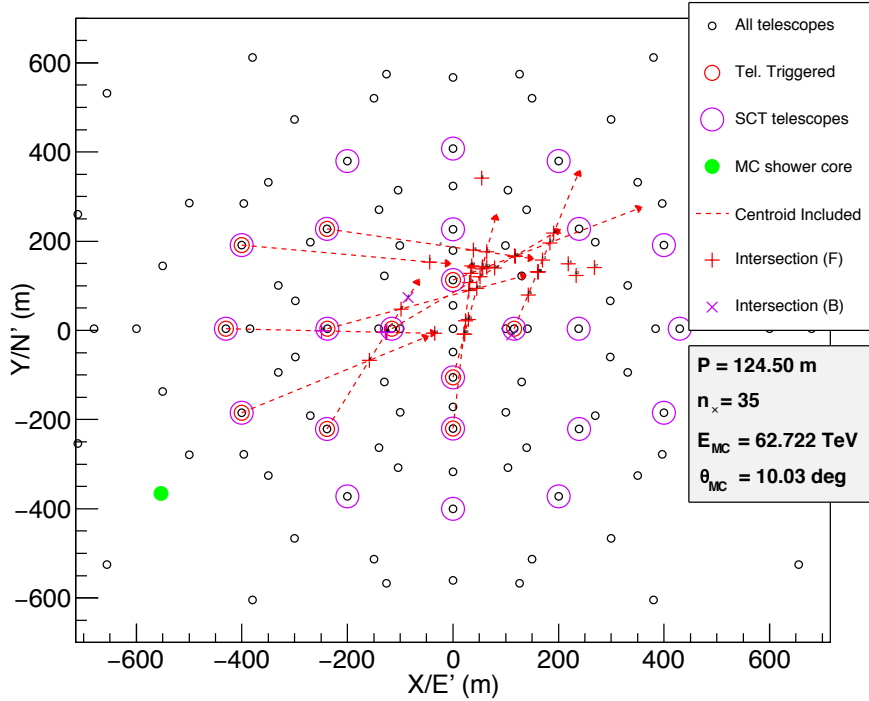


Figure 5: Array mirror plane projections illustrating P computation for an off-axis γ -ray event for $E_\gamma \gtrsim 2 \text{ TeV}$ (*top*), and an off-axis cosmic-ray proton event (*bottom*). See Figure 4 for an explanation of the event-specific quantities that each marker is used to indicate.

jected into the camera plane’s coordinate system¹⁰. Consequently, the derived $\{\mathbf{r}'_{\times,j}\}$ coincide closely with the projection of the axis into the array mirror plane. The *lower* panel of Figure 4 is representative of an *off-axis* γ -ray event with energy *below* 2 TeV. Low energy events typically produce compact camera images with small offsets between the true image centroid and that of the Boolean-valued trigger image. Accordingly, the projected point pairs connected by each of the \mathbf{r}'_F remain *almost* identical for all telescopes and the tight clustering of $\{\mathbf{r}'_{\times,j}\}$ is preserved. The arbitrary, *a-priori* definition of \mathbf{r}^* implies that the single, infinitely distant point that is projected to those camera-coordinates for *all* telescopes will *generally not* lie on the air shower axis. Accordingly, the coincidence between the $\{\mathbf{r}'_{\times,j}\}$ and the mirror-plane projection of the air-shower axis is lost. A more detailed discussion of this effect, as well as some additional considerations that apply to higher energy off-axis gamma-ray events, is presented in §4.

Finally, the *lower* panel of Figure 5 illustrates a proton-initiated event. There is now no guarantee that $\mathbf{r}_{C,i}$ for each telescope corresponds with the projection of a single 3-dimensional point, since different telescopes may image multiple, different sub-showers of the hadronic cascade. Accordingly, the tight clustering of the $\{\mathbf{r}'_{\times,j}\}$ is lost and the computed value of P is large.

4. Indiscriminate Acceptance for High-Energy Events

The parallax width algorithm assumes that the centroids of *trigger* images reliably encode the geometry of the air-showers. If the intensity profile of the Cherenkov light image is substantially assymmetric, the validity of this assumption may degrade. Ideally, the trigger-image centroid $\mathbf{r}_{C,i}$ should correspond closely with the *full image centroid* $\mathbf{r}_{C^\dagger,i}$, defined as the signal-amplitude-weighted mean position of all *imaging* pixels that trigger in response to incident Cherenkov photons. Without access to the information provided by the individual pixel *amplitudes*, the Boolean-valued *trigger* images appear more symmetric and the $\mathbf{r}_{C,i}$ that are used to compute P may not accurately represent the air-shower geometry.

The *left* and *right-hand* panels of Figure 1 illustrate schematically how any camera-coordinate offsets $\epsilon_{C,i} = \mathbf{r}_{C,i} - \mathbf{r}_{C^\dagger,i}$ between the two centroid definitions produce corresponding directional perturbations of each $\mathbf{r}_{F,i}$. A representative mirror-plane projection of these misaligned vectors is illustrated in the *top panel* of Figure 5, and yields a set $\{\mathbf{r}'_{F,i}\}$ that typically increases the dispersion between the $\{\mathbf{r}'_{\times,j}\}$ intersection coordinates, and inflates the computed value of P . The potential magnitude of $\epsilon_{C,i}$ increases for high-energy γ -ray-initiated air showers, which

¹⁰All points along the event’s arrival direction-vector are implicitly on the *air-shower axis* and that \mathbf{r}^* corresponds to the projection of the point on that vector that is located at infinity

typically produce extensive images that comprise a large number (n_{TP}) of triggered super-pixels.

To prevent spurious rejection of *genuine* high-energy, γ -ray-initiated events, a pre-calibrated multiplicity threshold $n_{\text{TP}} = n_{\text{TP}}^{\text{pass}}$ is used to unconditionally accept (or *pass through*) events for which **any** telescope in the array captures a trigger image comprising $n_{\text{TP}}^{\text{pass}}$ or more super-pixels. As illustrated by Figure 6, the expected *single-telescope* trigger rate R_p for simulated, *proton*-initiated air-showers is used to calibrate an appropriate value for $n_{\text{TP}}^{\text{pass}}$. To retain effective suppression of the most frequent cosmic-ray triggers, a threshold corresponding to the typical super-pixel multiplicity for *proton*-initiated events that trigger at 3% of the peak single-telescope rate is adopted. Data will be serialized and readout will occur for any telescope that records an image with $n_{\text{TP}} > n_{\text{TP}}^{\text{pass}}$. Accordingly, in order to select a threshold that effectively controls the single telescope dead time induced by cosmic-ray events that fulfill the pass-through criterion, it is important to calibrate $n_{\text{TP}}^{\text{pass}}$ using the differential trigger rate for a *single* telescope.

5. Hardware Implementation of the Parallax Width Algorithm

The simplicity of the algorithm that calculates P was intentionally designed to facilitate rapid, FPGA-based computation (See e.g. Anderson et al., 2008; Zitzer, 2013, for examples of existing VHE γ -ray telescopes that use similar technology). Rapid exchange of locally synthesized trigger-images and high-resolution timing data between nearby telescopes can be used to derive independent, telescope-specific values of P that can inform the decision to initiate or veto readout of finely pixelated image data. The ability to intelligently filter events before they are fully digitized, transmitted and stored substantially reduces the system deadtime that would be associated with those processes. We note that the parallax width veto does not completely eliminate system dead time, since events that are *accepted* by the array trigger will still require digitization and readout.

The design of the SCT prototype includes a 16 μs pixel readout buffer (Otte et al., 2015; Tibaldo et al., 2015), which exceeds the combined time required to exchange data between telescopes and compute P , enabling high-resolution signal data to be temporarily stored by each telescope pending a trigger decision. Hardware and firmware that implement the DIAT triggering scheme have also been developed and will be deployed concurrently with the SCT prototype. Hardware-based computation of P by direct evaluation of (1) is not practical. A proven alternative approach entails straightforward combination of values that are extracted from precomputed lookup tables (e.g. Anderson et al., 2008; Zitzer, 2013). Moreover, provided with appropriately parameterised tables, factors that complicate the computation, such as telescope field rotation or

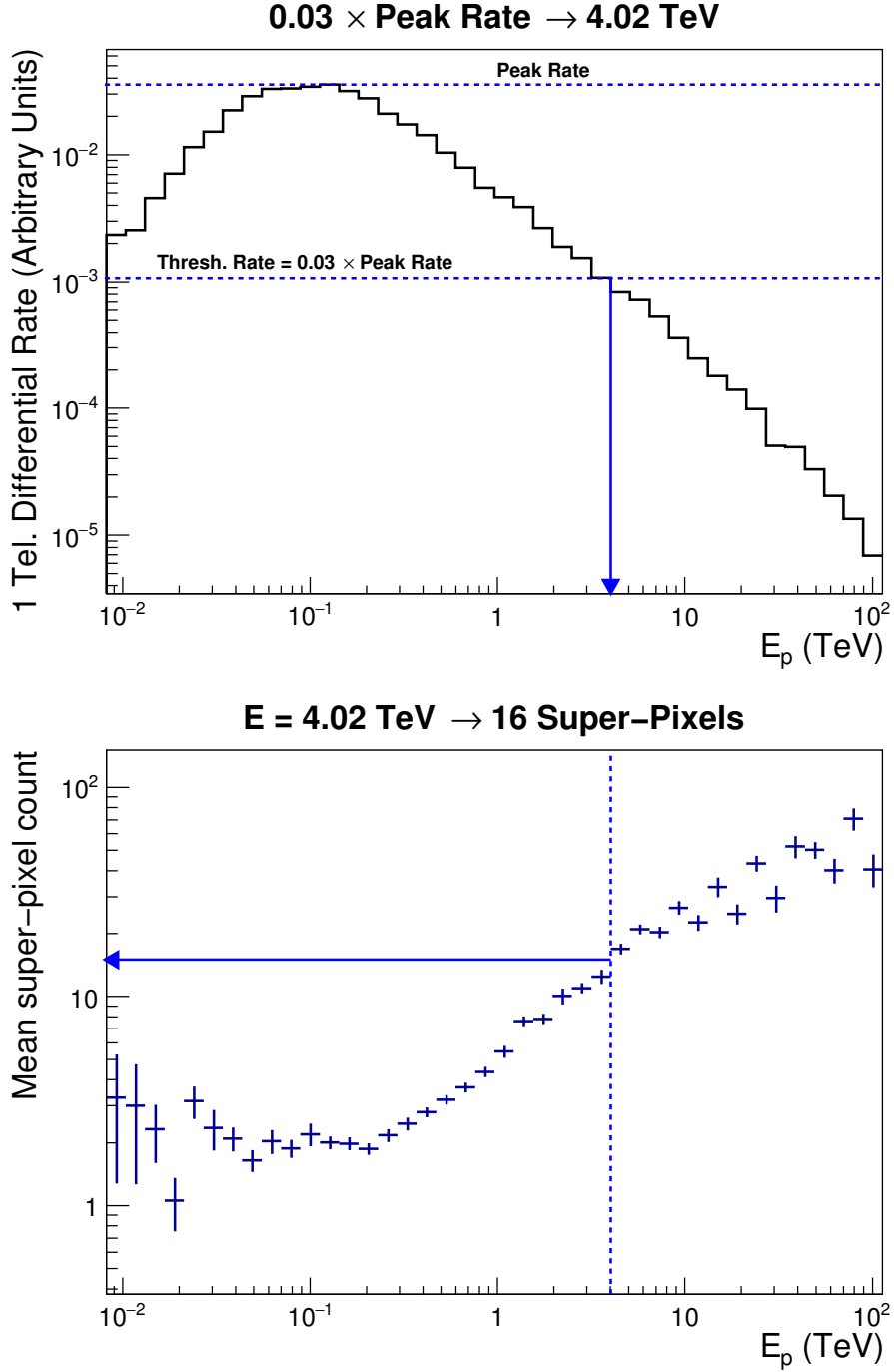


Figure 6: Computation of the super-pixel multiplicity $n_{\text{TP}}^{\text{pass}}$ that is required to satisfy the pass-through criterion. In the *top* panel, the energy-binned effective collection area for *proton*-initiated events that trigger *at least one* telescope is folded with the expected cosmic ray spectral shape ($\propto E_p^{-2.7}$) and used to determine the typical proton energy $E_{p,3\%}$ at which the expected rate of *single* telescope triggers falls below 3% of its peak value. Note that γ -ray-like images of a hadronic sub-shower typically sample a fraction of the energy of the incident proton. Accordingly, genuine γ -rays that produce images comprising $n_{\text{TP}}^{\text{pass}}$ trigger pixels have energies that are typically $\sim 30\%$ that of protons that do so. In the *bottom* panel, the energy-binned distribution of mean trigger image super-pixel multiplicities is used to derive the value of $n_{\text{TP}}^{\text{pass}}$ that corresponds to events for which $E_p \sim E_{p,3\%}$.

structural deformation under slewing, can be effectively addressed.

6. Results and Discussion

Figure 7 (*top*) shows the three distributions of P values that are computed for each investigated dataset, while the *bottom* panel displays the corresponding cumulative distributions for P . For the point-like γ -ray source, all the simulated photons are incident on-axis, and 90% of computed P values are < 11 m, in accordance with expectation. For extended and diffuse γ -ray sources, the majority of incident photons are incident off-axis. Nonetheless, the expected prevalence of small P values is realized, with 90% of events that do *not* fulfil the pass-through criterion having $P < 40$ m. In contrast $\sim 93\%$ of all proton-initiated events yield $P > 40$ m, confirming the expectation that P is a highly efficient discriminator between γ -ray- and proton-initiated events.

Figure 8 illustrates the evolution of γ -ray event retention with increasing angular offset θ_{off} between the assumed γ -ray incidence direction and the telescope optical axis. A point-like γ -ray source was simulated at various offsets from the camera centre and the resultant data were used to derive the threshold parallax width value of P_{th} that *retains* 90% of events which yield three valid trigger images. The expected energy dependence of P_{th} (see §4 for details) is evident, with event retention degrading most rapidly at large offsets for γ -ray energies exceeding 10 TeV but remaining $\lesssim 40$ m for $E_{\gamma} < 1$ TeV. Critically, the lowest energy event subset is characterized by the faintest Cherenkov images and therefore overlaps significantly with the set of events for which *none* of the triggering telescopes fulfill the pass-through criterion ($n_{\text{TP}}^{\text{pass}} = 16$). An important corollary is that those higher energy, large-offset events that *would* have been rejected on the basis of P alone are retained if the pass-through criterion is respected.

For the simulated array, indiscriminately accepting all events that fulfill the pass-through criterion, and adopting a $P_{\text{th}} = 40$ m for the remainder results in retention of $\gtrsim 90\%$ of genuine γ -ray events for $\theta_{\text{off}} \lesssim 3.5^\circ$.

Figure 9 illustrates how the rate of background-induced telescope triggers increases as the super-pixel trigger threshold is reduced. The rates were derived using simulations of proton-initiated air showers and random incidence of NSB photons upon each camera pixel is modelled by the detector simulation software. Individual curves represent the frequency of single-telescope triggers that are subsequently retained by a particular array triggering strategy. The requirement for retention by an array trigger implies a direct correspondence between the derived rates and the average frequency with which readout of finely pixelated image data would be initiated for each telescope.

The upper four curves in Figure 9 share a number of distinctive characteristics. For small n_{pe} , the majority of single telescope triggers are induced by random triggering

of camera pixels by NSB photons. The probability that random pixel triggers will generate a valid telescope trigger decreases rapidly with increasing n_{pe} and the resultant rate curve is characterized by a steeply falling power law. An *inflection point* marked by a reduction of the absolute power law index at a particular threshold (n_{pe}^*) represents the transition to a regime in which Cherenkov photons from cosmic-ray-induced air showers dominate the single telescope trigger rates. Whereas the incident flux of cosmic rays is typically stable and isotropic for a particular telescope location, the NSB intensity can vary markedly between different astronomical fields, and sporadic ambient light sources may also illuminate telescopes without warning. Figure 9 illustrates that without an array trigger, reliably stable operation would require $n_{\text{pe}}^{*,1\text{-fold}} \gtrsim 3.5$ p.e.. Relative to this threshold, *any* array trigger schemes enable reduction of n_{pe}^* and thereby reduce the threshold energy of γ -rays that the instrument can detect. Moreover, while traditional 2- and 3-fold multiplicity array triggers yield $n_{\text{pe}}^{*,2\text{-fold}} \approx 3.0$ p.e. and $n_{\text{pe}}^{*,3\text{-fold}} \approx 2.7$ p.e., a simulated array trigger that implements the parallax width algorithm and unconditionally accepts events that fulfill $n_{\text{TP}} \geq 16$, lowers the threshold at which the inflection point occurs to $n_{\text{pe}}^* \approx 2.5$ p.e. Specifying a pixel threshold n_{pe} that exceeds n_{pe}^* by factors of at least a few enables stable array operation in all but the most extreme observational conditions, but sacrifices sensitivity to intrinsically faint, low-energy γ -ray events. By substantially reducing n_{pe}^* , the parallax width trigger algorithm also lowers the overall energy threshold of the instrument.

In addition to providing efficient rejection of unwanted background events, the parallax width algorithm must also retain a large fraction of genuine γ -ray events. The *top* panel of Figure 10 illustrates the degree to which this is requirement is fulfilled by plotting the energy-binned effective collection areas for the simulated array configuration, assuming a point-like γ -ray source, *without* application of a pass-through for events yielding extensive high-multiplicity trigger images. The parallax width algorithm requires at least two intersections (and therefore three triggering telescopes) to compute P . Air showers with a lower overall energy content produce less Cherenkov light and consequently, they trigger fewer telescopes. Accordingly, although the parallax-width algorithm operates effectively for images that are not minimally reconstructible, the effective collection area for a two-telescope, minimally reconstructible image criterion (*green dashed* curves in Figure 10 and the *top* panel of Figure 11) nonetheless exceeds that of the parallax-width algorithm at energies below ~ 300 GeV. However, it should be noted that the ability to exploit images that are not minimally reconstructible enables the parallax width algorithm to retain *all* fully reconstructible three-telescope triggers at *all* energies. The *bottom* panel of Figure 10 demonstrates that adoption of a pass-through threshold $n_{\text{TP}}^{\text{pass}} = 16$ further enhances the retention of minimally reconstructible γ -ray events by the DIAT. We use *minimally reconstructible* to describe those

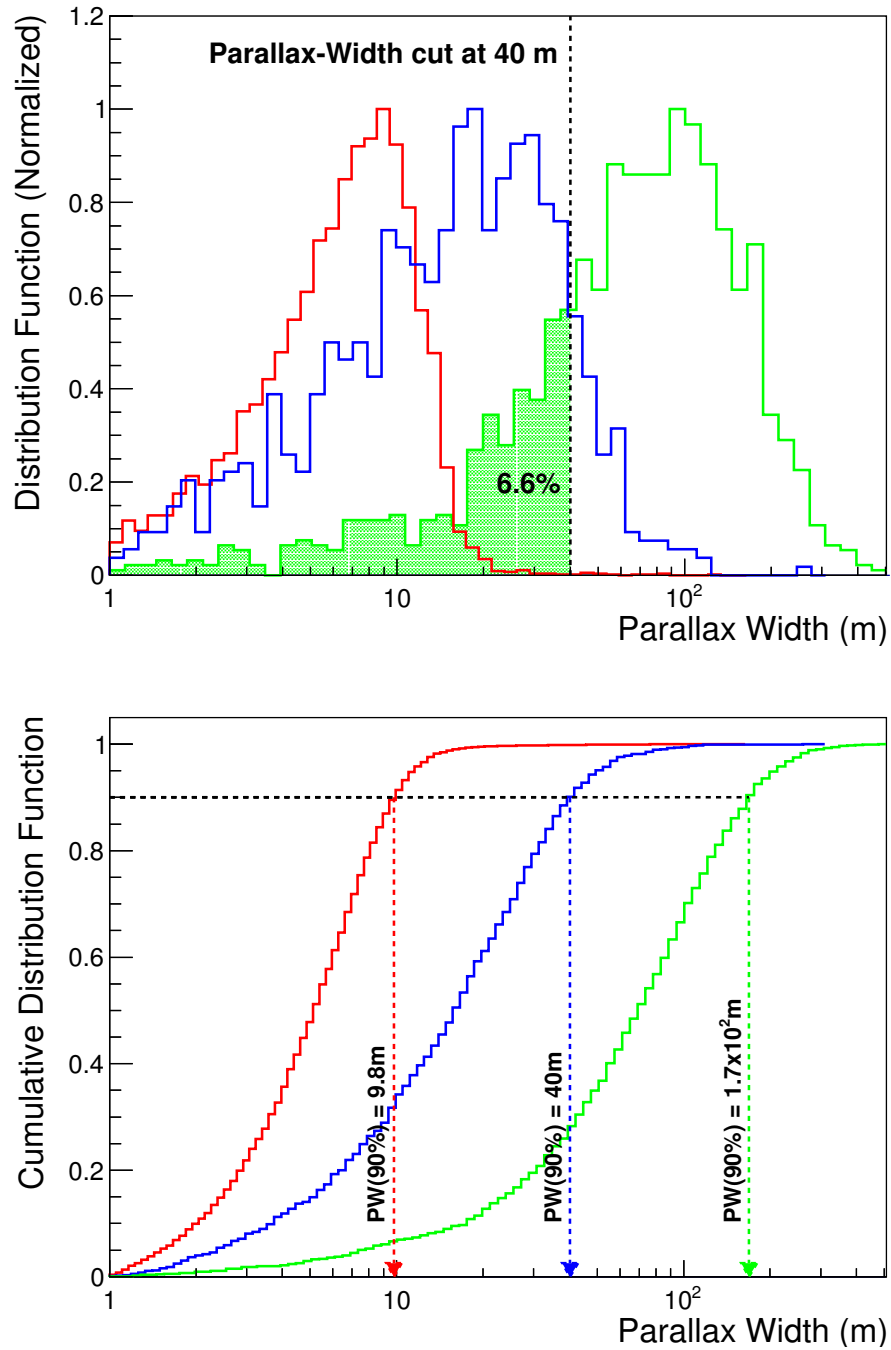


Figure 7: The computed distributions (*top*) and CDFs (*bottom*) of P values corresponding to point-origin (on-axis, *red*) and diffuse (*blue*) γ -ray events, and diffuse cosmic-ray background events (*green*).

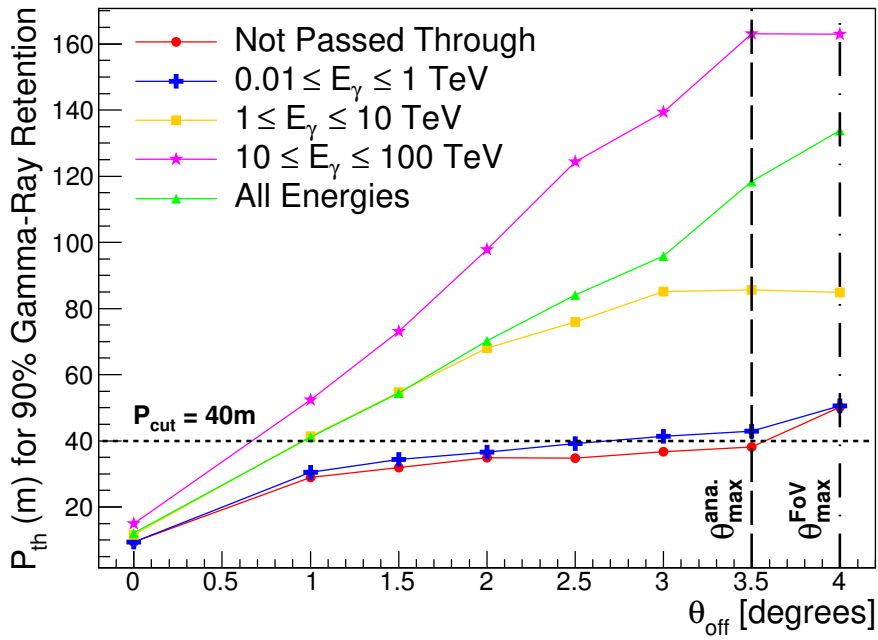


Figure 8: Evolution of γ -ray retention with increasing angular offset θ_{off} between the common optical axes of all telescopes in the array and true air-shower axis. The various curves represent different subsets of the simulated event ensemble and illustrate the threshold value $P_{\text{th}}(\theta_{\text{off}})$ below which 90% of γ -rays that trigger *at least three* telescopes in the array are retained by the selection algorithm. The *red* curve corresponds to predominantly low-energy γ -ray events that would **not** fulfill the pass-through array trigger criterion. The *blue*, *yellow* and *magenta* curves represent energy-selected subsets and illustrate that γ -ray retention at large offsets degrades with increasing γ -ray energy (E_γ). Finally, the *green* curve represents the union of the energy-selected subsets. Reliable reconstruction of events that are incident at offsets in excess of $\theta_{\text{max}}^{\text{ana.}} = 3.5^\circ$ (*dashed vertical line*) is typically problematic and such events would be discarded by subsequent data analysis. The *dot-dashed vertical* indicates the angular extent ($\theta_{\text{max}}^{\text{FoV}} = 4^\circ$) of the SCT camera.

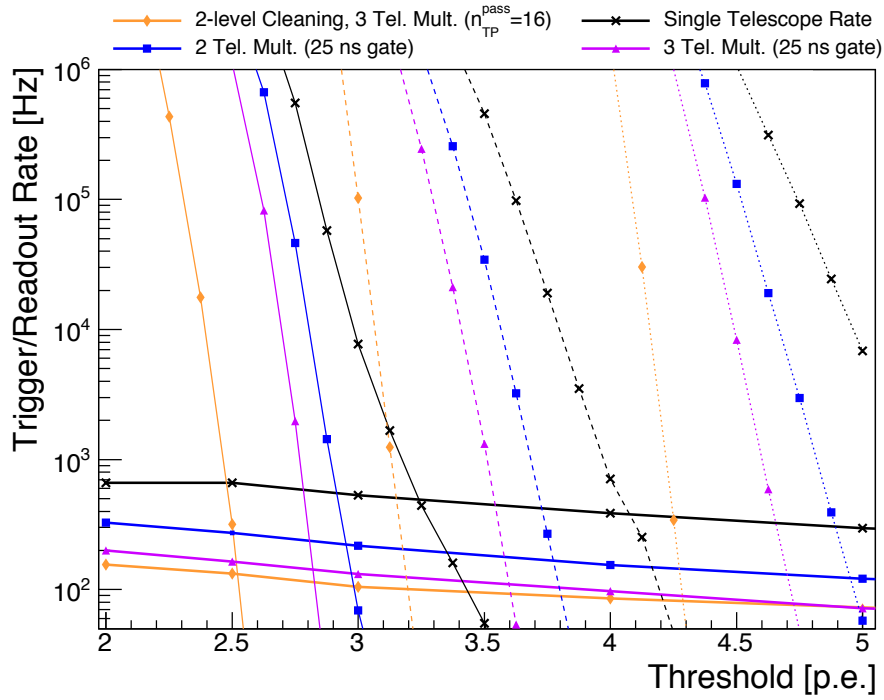


Figure 9: Projected *single telescope* readout rates following cosmic-ray or NSB-induced array triggers for various simulated super-pixel trigger thresholds. The expected array trigger rate in the absence of a multi-telescope trigger criterion is illustrated by the *black crosses*. The *blue squares* are derived by requiring that *at least* two telescopes in the array trigger within 25 ns, while *magenta triangles* illustrate the effect of increasing the telescope multiplicity requirement from two to three. *Orange diamonds* illustrate rates that result when the requirement that *at least* three telescopes trigger within 25 ns is retained before application of the two-level cleaning algorithm and subsequent indiscriminate acceptance of events with $n_{TP} \geq 16$. *Thick, solid curves* indicate the expected readout rate of cosmic-ray-proton-induced triggers. The remaining curves illustrate the expected readout rate of NSB-induced triggers for nominal (*thin solid lines*), two-times-nominal (*dashed lines*) and four-times-nominal (*dotted lines*) NSB intensity levels. The nominal NSB level implies production of 11.96 photoelectrons per super-pixel, per microsecond, which is consistent with a typical extragalactic field of view.

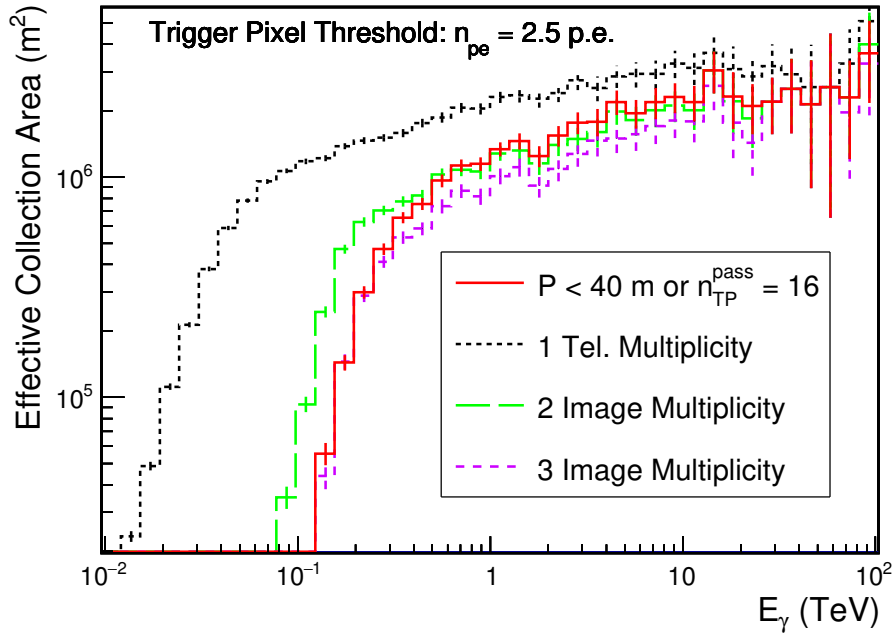
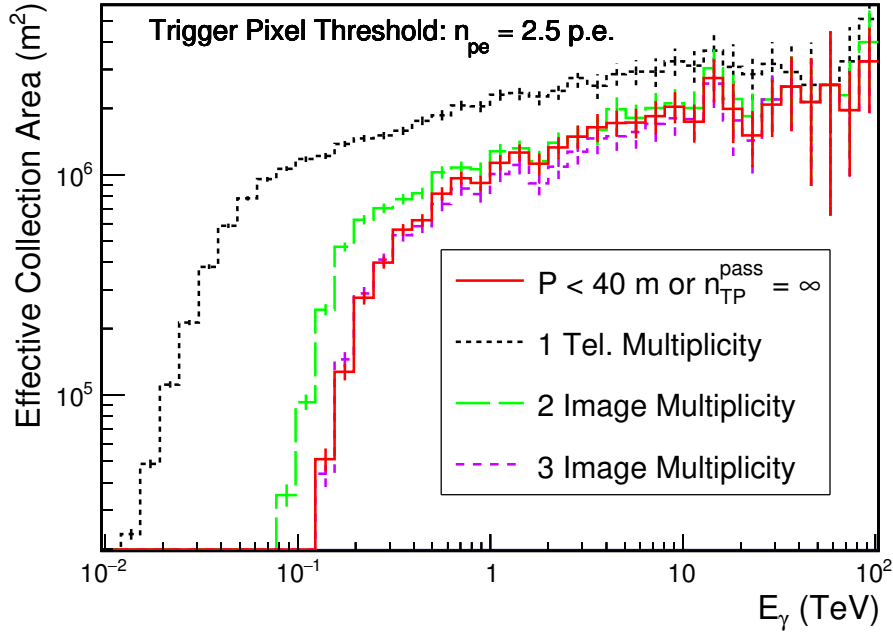


Figure 10: Collection areas for a point-origin γ -ray source and a super-pixel trigger threshold of 2.5 p.e. assuming $n_{TP}^{pass} \rightarrow \infty$ (*top*), and $n_{TP}^{pass} = 16$ (*bottom*). The *black* curve represents a single telescope trigger requirement (i.e. no array trigger). The *green* curve plots the collection area for events that trigger at least two telescopes and are subsequently found to yield two Cherenkov images that are useable for parameterization and geometric reconstruction of the corresponding air shower and the properties of its progenitor γ -ray. The *violet* curve illustrates the collection area for a more desirable subset of events that yield *at least three* high-quality Cherenkov images. The *red* curve represents the collection area for events that are accepted after application of the parallax width criterion, rejecting any events for which $P > 40$ m.

events that trigger at least two telescopes and are subsequently found to yield at least two Cherenkov images that are useable for parameterization and geometric reconstruction of the corresponding air shower and the properties of its progenitor γ -ray.

The *top* panel of Figure 11 uses simulated effective collection areas to demonstrate the response of the DIAT that implements the parallax width algorithm for a diffuse astrophysical γ -ray source, adopting $n_{\text{TP}}^{\text{pass}} = 16$. Hereafter, we describe images that can be used for parameterization and geometric reconstruction of the corresponding air shower and the properties of its progenitor γ -ray as *high quality*. At low energies the rejection of events yielding $P > 40\text{m}$ retains a large fraction of events that yield three high-quality Cherenkov images, while at energies $\gtrsim 1\text{ TeV}$, the pass-through trigger results in retention of *all* minimally reconstructible events. The *bottom* panel of Figure 11 illustrates the power of P to effectively reject cosmic-ray proton-initiated events. The *blue* curve illustrates the expected camera readout rate as a function of proton energy for a traditional two-telescope multiplicity array trigger, that accepts events for which at least two neighbouring telescopes trigger. The parallax width trigger reduces the expected rate of incorrectly accepted CR events by a factor of ~ 4 , which is almost double the suppression that is achieved by the two-telescope multiplicity requirement. Moreover, the contrast in CR suppression efficacy is maximized at lower energies where the incident cosmic ray rate is largest.

Figure 12 illustrates how a DIAT using the parallax width algorithm can be used to improve the low-energy sensitivity of the SCT subarray. Field-to-field variability of the NSB intensity between observations can induce unpredictable spikes in the array trigger rate if accidental coincidences between spurious single telescope triggers cannot be effectively suppressed. Typically, the required suppression is achieved by requiring a higher single-pixel trigger threshold, which increases the overall low-energy threshold of the array. The ability of the DIAT to perform real-time multi-telescope event vetoing allows lower pixel thresholds to be used while maintaining tractable array trigger rates. In Figure 12 (*top panel*), the differential trigger rates for a Crab-pulsar-like γ -ray source are compared for minimally reconstructible events that satisfy $P < 40\text{m}$ assuming a trigger pixel threshold of 2.5 p.e., with the set of minimally reconstructible events that fulfil a traditional two-telescope multiplicity array trigger with $n_{\text{pe}} = 3.5\text{ p.e.}$. The lower pixel threshold made feasible by a hardware-level DIAT yields a substantial improvement in sensitivity below 200 GeV, achieving a factor of ~ 4 enhancement in collection area at the lowest energies.

7. Summary

Monte-Carlo simulations that model an array of SC Cherenkov Telescopes have been used to demonstrate that efficient rejection of cosmic-ray-initiated events is possible

using an innovative, distributed, intelligent array trigger. The simulated trigger implements an algorithm (designated *Parallax Width*) that performs hardware-level analysis using computed moments of the Cherenkov light distributions that are imaged by multiple telescopes. It successfully discriminates between background and genuine γ -ray triggers, while retaining a large majority of reconstructible events.

Simulated application of a DIAT that implements the *Parallax Width* algorithm demonstrated several advantages over arrays that utilize traditional *telescope multiplicity* triggers or operate without an array trigger.

- By vetoing spurious single and multiple telescope triggers before data are read out, the algorithm reduces the array trigger rate by a factor of ~ 7 . This enables finely sampled events with heavy data payloads to be generated by participating SCTs without overwhelming the array data transfer infrastructure.
- Real-time consideration of data from multiple telescopes also allows the rate of NSB-induced array triggers to be controlled without increasing the super-pixel trigger thresholds. Indeed, a reduction in super-pixel trigger threshold corresponding to an additional photoelectron-equivalent count is rendered feasible.
- The resultant enhancement of low-energy sensitivity increases the number of reconstructible events with energies between $\sim 100\text{ GeV}$ and $\sim 200\text{ GeV}$, which may be particularly useful for studies of spectrally soft targets like the Crab pulsar.

The configuration of the simulated telescope array represents a realistic scenario but was *not* tailored to maximize the efficacy of the parallax width trigger algorithm. Accordingly, a suitably optimized telescope array is likely to realize additional improvements in overall performance.

8. Acknowledgements

The authors thank Dr Michael Punch, Dr John Ward, and Dr Matthew Wood for the valuable advice and insight they provided with regard to this study. This paper has gone through internal review by the CTA Consortium.

References

- Acero, F., Ackermann, M., Ajello, M., Albert, A., Atwood, W. B., Axelsson, M., Baldini, L., Ballet, J., Barbiellini, G., Bastieri, D., Belfiore, A., Bellazzini, R., Bissaldi, E., Blandford, R. D., Bloom, E. D., Bogart, J. R., Bonino, R., Bottacini, E., Bregeon, J., Britto, R. J., Bruel, P., Buehler, R., Burnett, T. H., Buson, S., Caliendo, G. A., Cameron, R. A., Caputo, R., Caragiulo, M., Caraveo, P. A., Casandjian, J. M., Cavazzuti, E., Charles, E., Chaves, R. C. G., Chekhtman, A., Cheung, C. C., Chiang, J., Chiaro, G., Ciprini, S., Claus, R., Cohen-Tanugi, J., Cominsky, L. R., Conrad, J., Cutini, S., D’Ammando, F., de Angelis, A., DeKlotz, M., de Palma, F., Desiante, R., Digel, S. W., Di Venere, L., Drell, P. S., Dubois, R., Dumora, D., Favuzzi, C., Fegan, S. J., Ferrara, E. C., Finke,

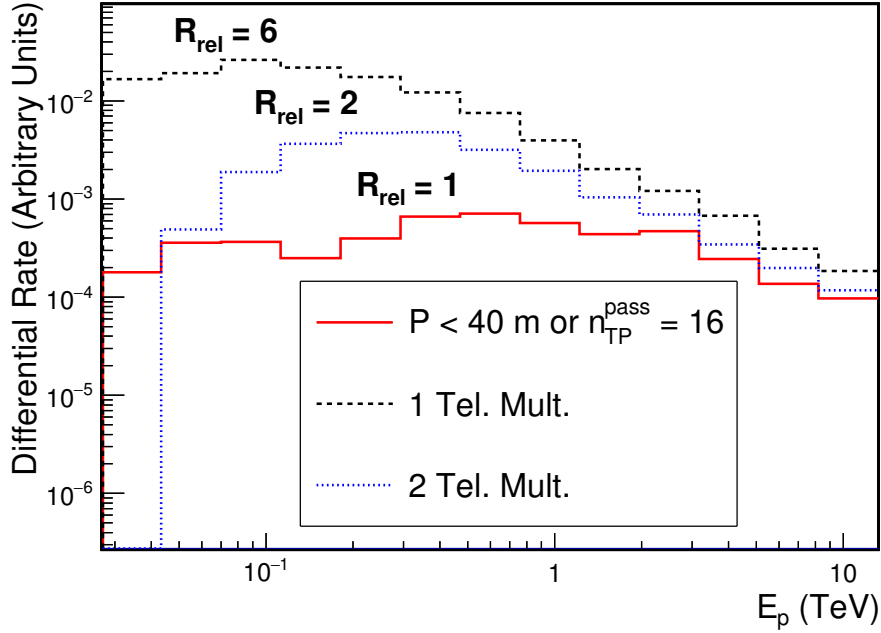
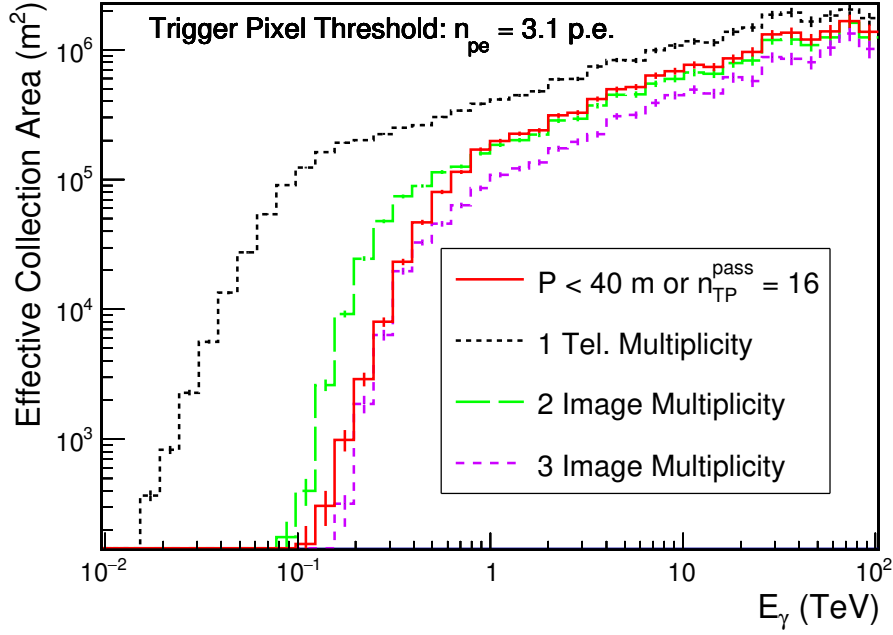


Figure 11: *Top panel:* Collection areas for diffuse γ -ray emission that correspond to different array triggering strategies, assuming a super-pixel trigger threshold of 2.5 p.e. and $n_{\text{TP}}^{\text{pass}} = 16$. See Figure 10 for a detailed description of the criteria used to generate each curve. *Bottom panel:* Differential readout rates induced by diffuse proton events for different array-triggering scenarios. The *black dashed* curve illustrates the single telescope readout rate, in the absence of any array trigger. The *blue dotted* curve represents the rate at which two telescopes trigger coincidentally and initiate camera readout. The *solid red* curve illustrates the collection area for events that are accepted by an array trigger implementing the parallax width algorithm with $P < 40$ m, assuming a super-pixel trigger threshold of 2.5 p.e. and reveals the additional vetoing of proton initiated events that is achieved. Each curve is annotated with the relative *integral* readout rates, using the parallax width array trigger as the fiducial case. *Both panels* correspond to a pass-through super-pixel multiplicity threshold $n_{\text{TP}}^{\text{pass}} = 16$.

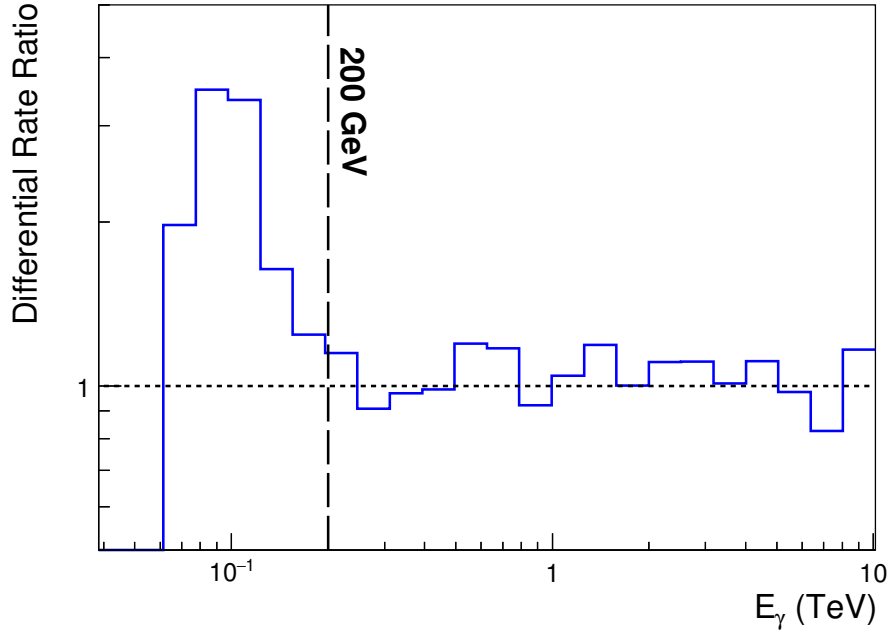
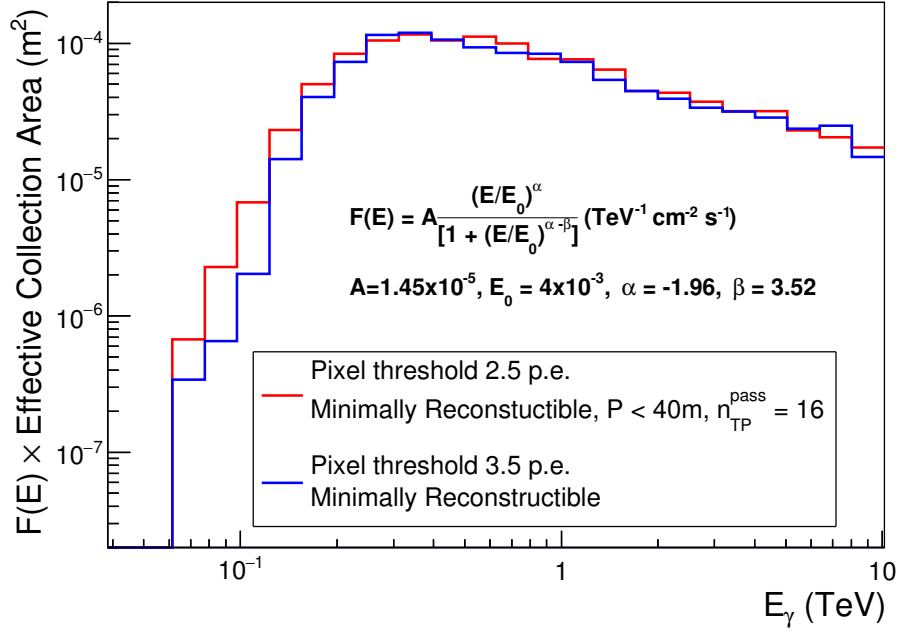


Figure 12: The expected array trigger rates for on-axis γ -ray-initiated events are shown in the *top panel* for a Crab-pulsar-like spectral shape. The red curve corresponds to minimally reconstructible events that are retained after application of a trigger threshold corresponding to 2.5 p.e. per super-pixel, and subsequent filtering using the parallax width algorithm with $P < 40\text{m}$, and a pass-through threshold $n_{\text{TP}}^{\text{pass}} = 16$. For comparison, the blue curve plots the expected array rate for minimally reconstructible events, assuming a higher super-pixel threshold of 3.5 p.e., which is typically required to ensure stable operation under variable NSB illumination without an array trigger. The ratio of the red and blue curves is shown in the *bottom panel* and illustrates that application of the parallax width discriminator enables effective recovery of low energy events by rendering a lower super-pixel threshold feasible.

J., Franckowiak, A., Fukazawa, Y., Funk, S., Fusco, P., Gargano, F., Gasparri, D., Giebels, B., Giglietto, N., Giommi, P., Giordano, F., Giroletti, M., Glanzman, T., Godfrey, G., Grenier, I. A., Grondin, M.-H., Grove, J. E., Guillemot, L., Guiriec, S., Hadasch, D., Harding, A. K., Hays, E., Hewitt, J. W., Hill, A. B., Horan, D., Iafrate, G., Jogler, T., Jóhannesson, G., Johnson, R. P., Johnson, A. S., Johnson, T. J., Johnson, W. N., Kamae, T., Kataoka, J., Katsuta, J., Kuss, M., La Mura, G., Landriau, D., Larsson, S., Latronico, L., Lemoine-Goumard, M., Li, J., Li, L., Longo, F., Loparco, F., Lott, B., Lovellette, M. N., Lubrano, P., Madejski, G. M., Massaro, F., Mayer, M., Mazziotta, M. N., McEnery, J. E., Michelson, P. F., Mirabal, N., Mizuno, T., Moiseev, A. A., Mongelli, M., Monzani, M. E., Morselli, A., Moskalenko, I. V., Murgia, S., Nuss, E., Ohno, M., Ohsugi, T., Omodei, N., Orienti, M., Orlando, E., Ormes, J. F., Paneque, D., Panetta, J. H., Perkins, J. S., Pesce-Rollins, M., Piron, F., Pivato, G., Porter, T. A., Racusin, J. L., Rando, R., Razzano, M., Razaque, S., Reimer, A., Reimer, O., Reposeur, T., Rochester, L. S., Romani, R. W., Salvetti, D., Sánchez-Conde, M., Saz Parkinson, P. M., Schulz, A., Siskind, E. J., Smith, D. A., Spada, F., Spandre, G., Spinelli, P., Stephens, T. E., Strong, A. W., Suson, D. J., Takahashi, H., Takahashi, T., Tanaka, Y., Thayer, J. G., Thayer, J. B., Thompson, D. J., Tibaldo, L., Tibolla, O., Torres, D. F., Torres, E., Tosti, G., Troja, E., Van Klaveren, B., Vianello, G., Winer, B. L., Wood, K. S., Wood, M., Zimmer, S., Fermi-LAT Collaboration, Jun. 2015. Fermi Large Area Telescope Third Source Catalog. ApJS218, 23.

Acharya, B., Actis, M., Aghajani, T., Agnetta, G., Aguilar, J., Aharonian, F., Ajello, M., Akhperjanian, A., Alcubierre, M., Aleksi, J., Alfaro, R., Aliu, E., Allafort, A., Allan, D., Allekotte, I., Amato, E., Anderson, J., Angner, E., Antonelli, L., Antoranz, P., Aravantinos, A., Arlen, T., Armstrong, T., Arnaldi, H., Arrabito, L., Asano, K., Ashton, T., Asorey, H., Awane, Y., Baba, H., Babic, A., Baby, N., Bahr, J., Bais, A., Baixeras, C., Bajtlik, S., Balbo, M., Balis, D., Balkowski, C., Bamba, A., Bandiera, R., Barber, A., Barbier, C., Barcel, M., Barnacka, A., Barnstedt, J., de Almeida, U. B., Barrio, J., Basili, A., Basso, S., Bastieri, D., Bauer, C., Baushev, A., Becerra, J., Becherini, Y., Bechtol, K., Tjus, J. B., Beckmann, V., Bednarek, W., Behera, B., Belluso, M., Benbow, W., Berdugo, J., Berger, K., Bernard, F., Bernardino, T., Bernlhr, K., Bhat, N., Bhattacharyya, S., Bigongiari, C., Biland, A., Billotta, S., Bird, T., Birsin, E., Bissaldi, E., Biteau, J., Bitossi, M., Blake, S., Bigas, O. B., Blasi, P., Bobkov, A., Boccone, V., Boettcher, M., Bogacz, L., Bogart, J., Bogdan, M., Boisson, C., Gargallo, J. B., Bolmont, J., Bonanno, G., Bonardi, A., Bonev, T., Bonifacio, P., Bonnoli, G., Bordas, P., Borgland, A., Borkowski, J., Bose, R., Botner, O., Bottani, A., Bouchet, L., Bourgeat, M., Boutonnet, C., Bouvier, A., Brau-Nogu, S., Braun, I., Bretz, T., Briggs, M., Bringmann, T., Brook, P., Brun, P., Brunetti, L., Buanes, T., Buckley, J., Buehler, R., Bugaev, V., Bulgarelli, A., Bulik, T., Busetto, G., Buson, S., Byrum, K., Cailles, M., Cameron, R., Camprecios, J., Canestrari, R., Cantu, S., Capalbi, M., Caraveo, P., Carmona, E., Carosi, A., Carr, J., Carton, P.-H., Casanova, S., Casiraghi, M., Catalano, O., Cavazzani, S., Cazaux, S., Cerruti, M., Chabanne, E., Chadwick, P., Champion, C., Chen, A., Chiang, J., Chiappetti, L., Chikawa, M., Chitnis, V., Chollet, F., Chudoba, J., Cielar, M., Cillis, A., Cohen-Tanugi, J., Colafrancesco, S., Colin, P., Colome, J., Colonges, S., Compin, M., Conconi, P., Conforti, V., Connaughton, V., Conrad, J., Contreras, J., Coppi, P., Corona, P., Corti, D., Cortina, J., Cossio, L., Costantini, H., Cotter, G., Courty, B., Couturier, S., Covino, S., Crimi, G., Criswell, S., Croston, J., Cusumano, G., Dafonseca, M., Dale, O., Daniel, M., Darling, J., Davids, I., Dazzi, F., Angelis, A. D., Caprio, V. D., Frondat, F. D., de Gouveia Dal Pino, E., de la Calle, I., Vega, G. D. L., de los Reyes Lopez, R., Lotto, B. D., Luca, A. D., de Mello Neto, J., de Naurois, M., de Oliveira, Y., de Oa Wilhelmi, E., de Souza, V., Decerprit, G., Decock, G., Deil, C., Delagnes, E., Deleglise, G., Delgado, C., Volpe, D. D., Demange, P., Depaola, G., Dettlaff, A., Paola, A. D., Pierro, F. D., Daz, C., Dick, J., Dickherber, R., Dickinson, H., Diez-Blanco, V., Digel, S., Dimitrov, D., Disset, G., Djannati-Ata, A., Doert, M., Dohmke, M., Domainko, W., Prester, D. D., Donat, A., Dorner, D., Doro, M., Dournaux, J.-L., Drake, G., Dravins, D., Drury, L., Dubois, F., Dubois, R., Dubus, G., Dufour, C., Dumas, D., Dumm, J., Durand, D., Dyks, J., Dyrda, M., Ebr, J., Edy, E., Egberts, K., Eger, P., Einecke, S., Eleftheriadis, C., Elles, S., Emmanoulopoulos, D., Engelhaupt, D., Enomoto, R., Ernenwein, J.-P., Errando, M., Etchegoyen, A., Evans, P., Falcone, A., Fantinel, D., Farakos, K., Farnier, C., Fasola, G., Favill, B., Fede, E., Federici, S., Fegan, S., Feinstein, F., Ferenc, D., Ferrando, P., Fesquet, M., Fiasson, A., Fillin-Martino, E., Fink, D., Finley, C., Finley, J., Fiorini, M., Curcoll, R. F., Flores, H., Florin, D., Focke, W., Fhr, C., Fokitis, E., Font, L., Fontaine, G., Fornasa, M., Frster, A., Fortson, L., Fouque, N., Franckowiak, A., Fransson, C., Fraser, G., Frei, R., Albuquerque, I., Fresnillo, L., Fruck, C., Fujita, Y., Fukazawa, Y., Fukui, Y., Funk, S., Gbele, W., Gabici, S., Gabriele, R., Gadola, A., Galante, N., Gall, D., Gallant, Y., Gmez-Garca, J., Garca, B., Lpez, R. G., Gardiol, D., Garrido, D., Garrido, L., Gascon, D., Gaug, M., Gaweda, J., Gebremedhin, L., Geffroy, N., Gerard, L., Ghedina, A., Ghigo, M., Giannakaki, E., Gianotti, F., Giarrusso, S., Giavitto, G., Giebels, B., Gika, V., Giommi, P., Girard, N., Giro, E., Giuliani, G., Glanzman, T., Glicenstein, J.-F., Godinovic, N., Golev, V., Berisso, M. G., Gmez-Ortega, J., Gonzalez, M., Gonzlez, A., Gonzlez, F., Muoz, A. G., Gothe, K., Gougerot, M., Graciani, R., Grandi, P., Graena, F., Granot, J., Grasseau, G., Gredig, R., Green, A., Greenshaw, T., Grgoire, T., Grimm, O., Grube, J., Grudzinska, M., Gruev, V., Grnewald, S., Grygorczuk, J., Guarino, V., Gunji, S., Gyuk, G., Hadasch, D., Hagiwara, R., Hahn, J., Hakansson, N., Hallgren, A., Heras, N. H., Hara, S., Hardcastle, M., Harris, J., Hassan, T., Hatanaka, K., Haubold, T., Haupt, A., Hayakawa, T., Hayashida, M., Heller, R., Henault, F., Henri, G., Hermann, G., Hermel, R., Herrero, A., Hidaka, N., Hinton, J., Hoffmann, D., Hofmann, W., Hofverberg, P., Holder, J., Horns, D., Horville, D., Houles, J., Hrabovsky, M., Hrupec, D., Huan, H., Huber, B., Huet, J.-M., Hughes, G., Humenys, T., Huovelin, J., Ibarra, A., Illa, J., Impiombato, D., Incorvaia, S., Inoue, S., Inoue, Y., Ioka, K., Ismailova, E., Jablonski, C., Jacholkowska, A., Jamroz, M., Janiak, M., Jean, P., Jeanney, C., Jimenez, J., Jogler, T., Johnson, T., Journet, L., Juffroy, C., Jung, I., Kaaret, P., Kabuki, S., Kagaya, M., Kakuwa, J., Kalkuhl, C., Kankanyan, R., Karastergiou, A., Krcher, K., Karczewski, M., Karkar, S., Kasperek, J., Kastana, D., Katagiri, H., Kataoka, J., Katarzyski, K., Katz, U., Kawanaka, N., Kellner-Leidel, B., Kelly, H., Kendziorra, E., Khelif, B., Kieda, D., Kifune, T., Kihm, T., Kishimoto, T., Kitamoto, K., Kluniak, W., Knapic, C., Knapp, J., Knldseeder, J., Kck, F., Kocot, J., Kodani, K., Khne, J.-H., Kohri, K., Kokkotas, K., Kolitzus, D., Komin, N., Kominis, I., Konno, Y., Kppel, H., Korohoda, P., Kosack, K., Koss, G., Kossakowski, R., Kostka, P., Koul, R., Kowal, G., Koyama, S., Koziol, J., Krhenbhl, T., Krause, J., Krawczynski, H., Krennrich, F., Krepps, A., Kretzschmann, A., Krobot, R., Krueger, P., Kubo, H., Kudryavtsev, V., Kushida, J., Kuznetsov, A., Barbera, A. L., Palombara, N. L., Parola, V. L., Rosa, G. L., Lacombe, K., Lamanna, G., Lande, J., Languignon, D., Lapington, J., Laporte, P., Lavalley, C., Flour, T. L., Padellec, A. L., Lee, S.-H., Lee, W., de Oliveira, M. L., Lelas, D., Lenain, J.-P., Leopold, D., Lerch, T., Lessio, L., Lieunard, B., Lindfors, E., Liolios, A., Lipniacka, A., Lockart, H., Lohse, T., Lombardi, S., Lopatin, A., Lopez, M., Lpez-Coto, R., Lpez-Oramas, A., Lorca, A., Lorenz, E., Lubinski, P., Lucarelli, F., Ldecke, H., Ludwin, J., Luque-Escamilla, P., Lustermaan, W., Luz, O., Lyard, E., Maccarone, M., Maccarone, T., Madejski, G., Madhavan, A., Mahabir, M., Maier, G., Majumdar, P., Malaguti, G., Maltezos, S., Manalaysay, A., Mancilla, A., Mandat, D., Maneva, G., Mangano, A., Manigot, P., Mannheim, K., Manthos, I., Maragos, N., Marcowith, A., Mariotti, M., Marisaldi, M., Markoff, S., Marszaek, A., Martens, C., Mart, J., Martin, J.-M., Martin, P., Martinez, G., Martinez, F., Martinez, M., Masserot, A., Mastichiadis, A., Mathieu, A., Matsumoto, H., Mattana, F., Mattiazzo, S., Maurin, G., Maxfield, S., Maya, J., Mazin, D.,

- Comb, L. M., McCubbin, N., McHardy, I., McKay, R., Medina, C., Melioli, C., Melkumyan, D., Mereghetti, S., Mertsch, P., Meucci, M., Michaowski, J., Micolon, P., Mihailidis, A., Mineo, T., Minuti, M., Mirabal, N., Mirabel, F., Miranda, J., Mirzoyan, R., Mizuno, T., Moal, B., Moderski, R., Mognet, I., Molinari, E., Molinaro, M., Montaruli, T., Monteiro, I., Moore, P., Olaizola, A. M., Mordalska, M., Morello, C., Mori, K., Mottez, F., Moudeden, Y., Moulin, E., Mrusek, I., Mukherjee, R., Munar-Adrover, P., Muraishi, H., Murase, K., Murphy, A., Nagasaki, S., Naito, T., Nakajima, D., Nakamori, T., Nakayama, K., Naumann, C., Naumann, D., Naumann-Godo, M., Nayman, P., Nedbal, D., Neise, D., Nellen, L., Neustroev, V., Neyroud, N., Nicastro, L., Nicolau-Kukliski, J., Niedwiecki, A., Niemiec, J., Nieto, D., Nikolaidis, A., Nishijima, K., Nolan, S., Northrop, R., Nosek, D., Nowak, N., Nozato, A., O'Brien, P., Ohira, Y., Ohishi, M., Ohm, S., Ohoka, H., Okuda, T., Okumura, A., Olive, J.-F., Ong, R., Orito, R., Orr, M., Osborne, J., Ostrowski, M., Otero, L., Otte, N., Ovcharov, E., Oya, I., Ozieblo, A., Padilla, L., Paiano, S., Paillet, D., Paizis, A., Palanque, S., Palatka, M., Pallota, J., Panagiotidis, K., Panazol, J.-L., Paneque, D., Panter, M., Paoletti, R., Papayannis, A., Papyan, G., Paredes, J., Pareschi, G., Parks, G., Parraud, J.-M., Parsons, D., Arribas, M. P., Pech, M., Pedalletti, G., Pelassa, V., Pelat, D., Perez, M., Persic, M., Petrucci, P.-O., Peyaud, B., Pichel, A., Pita, S., Pizzolato, F., Platos, ., Platzer, R., Pogosyan, L., Pohl, M., Pojmanski, G., Ponz, J., Potter, W., Poutanen, J., Prandini, E., Prast, J., Preece, R., Profeti, F., Prokoph, H., Prouza, M., Proyetti, M., Puerto-Gimenez, I., Phlhofer, G., Puljak, I., Punch, M., Pyzio, R., Quel, E., Quinn, J., Quirrenbach, A., Racero, E., Rajda, P., Ramon, P., Rando, R., Rannot, R., Rataj, M., Raue, M., Reardon, P., Reimann, O., Reimer, A., Reimer, O., Reitberger, K., Renaud, M., Renner, S., Reville, B., Rhode, W., Rib, M., Ribordy, M., Richer, M., Rico, J., Ridky, J., Rieger, F., Ringegni, P., Ripken, J., Ristori, P., Rivire, A., Rivoire, S., Rob, L., Roeser, U., Rohlfs, R., Rojas, G., Romano, P., Romaszkan, W., Romero, G., Rosen, S., Lees, S. R., Ross, D., Rouaix, G., Rousselet, J., Rousselet, S., Rovero, A., Roy, F., Royer, S., Rudak, B., Julien, C., Rupiski, M., Russo, F., Ryde, F., Sacco, B., Saemann, E., Saggion, A., Sahakian, V., Saito, K., Saito, T., Saito, Y., Sakaki, N., Sakonaka, R., Salini, A., Sanchez, F., Sanchez-Conde, M., Sandoval, A., Sandaker, H., SantAmbrogio, E., Santangelo, A., Santos, E., Sanuy, A., Sapozhnikov, L., Sarkar, S., Sartore, N., Sasaki, H., Satalecka, K., Sawada, M., Scalzotto, V., Scapin, V., Scarioffolo, M., Schafer, J., Schanz, T., Schlenstedt, S., Schlick-eiser, R., Schmidt, T., Schmoll, J., Schovaneck, P., Schroedter, M., Schultz, C., Schultze, J., Schulz, A., Schure, K., Schwab, T., Schwanke, U., Schwarz, J., Schwarzburg, S., Schweizer, T., Schwemmer, S., Segreto, A., Seiradakis, J.-H., Sembroski, G., Seweryn, K., Sharma, M., Shayduk, M., Shellard, R., Shi, J., Shibata, T., Shibuya, A., Shum, E., Sidoli, L., Sidz, M., Siewi, J., Sikora, M., Silk, J., Sillanp, A., Singh, B., Sitarek, J., Skole, C., Smareglia, R., Smith, A., Smith, D., Smith, J., Smith, N., Sobczyk, D., Sol, H., Sottile, G., Sowiski, M., Spanier, F., Spiga, D., Spyrou, S., Stamatescu, V., Stamerra, A., Starling, R., Stawarz, ., Steenkamp, R., Stegmann, C., Steiner, S., Stergioulas, N., Sternberger, R., Sterzel, M., Stinzing, F., Stodulski, M., Straumann, U., Strazzeri, E., Stringhetti, L., Suarez, A., Suchenek, M., Sugawara, R., Sulanke, K.-H., Sun, S., Supanitsky, A., Suric, T., Sutcliffe, P., Sykes, J., Szanecki, M., Szeplieniec, T., Szostek, A., Tagliaferri, G., Tajima, H., Takahashi, H., Takahashi, K., Takalo, L., Takami, H., Talbot, G., Tammi, J., Tanaka, M., Tanaka, S., Tazan, J., Tavani, M., Tavernet, J.-P., Tejedor, L., Teleshinsky, I., Temnikov, P., Tenzer, C., Terada, Y., Terrier, R., Teshima, M., Testa, V., Tezier, D., Thuermann, D., Tibaldo, L., Tibolla, O., Tiengo, A., Tluczykont, M., Peixoto, C. T., Tokanai, F., Tokarz, M., Toma, K., Torii, K., Tornikoski, M., Torres, D., Torres, M., Tosti, G., Totani, T., Toussnel, F., Tovmassian, G., Travnicek, P., Trifoglio, M., Troyano, I., Tsinganos, K., Ueno, H., Umehara, K., Upadhyay, S., Usher, T., Uslenghi, M., Valdes-Galicia, J., Vallania, P., Vallejo, G., van Driel, W., van Eldik, C., Vandenbrouke, J., Vanderwalt, J., Vankov, H., Vasileiadis, G., Vassiliev, V., Veberic, D., Vegas, I., Vercellone, S., Vergani, S., Veysire, C., Vialle, J., Viana, A., Videla, M., Vincent, P., Vincent, S., Vink, J., Vlahakis, N., Vlahos, L., Vogler, P., Vollhardt, A., von Gunten, H.-P., Vorobiov, S., Vuerli, C., Waeghebaert, V., Wagner, R., Wagner, R., Wagner, S., Wakely, S., Walter, R., Walther, T., Warda, K., Warwick, R., Wawer, P., Wawrzaszek, R., Webb, N., Wegner, P., Weinstein, A., Weitzel, Q., Welsing, R., Werner, M., Wetteskind, H., White, R., Wierzcholska, A., Wiesand, S., Wilkinson, M., Williams, D., Willingale, R., Winiarski, K., Wischnewski, R., Winiewski, ., Wood, M., Wrnlein, A., Xiong, Q., Yadav, K., Yamamoto, H., Yamamoto, T., Yamazaki, R., Yanagita, S., Yebras, J., Yelos, D., Yoshida, A., Yoshida, T., Yoshikoshi, T., Zabalza, V., Zacharias, M., Zajczyk, A., Zanin, R., Zdziarski, A., Zech, A., Zhao, A., Zhou, X., Zitara, K., Ziolkowski, J., Zikowski, P., Zitelli, V., Zurbach, C., ychowski, P., 2013. Introducing the {CTA} concept. *Astroparticle Physics* 43, 3 – 18, seeing the High-Energy Universe with the Cherenkov Telescope Array - The Science Explored with the {CTA}.
- URL <http://www.sciencedirect.com/science/article/pii/S0927650513000169>
- Acharya, B. S., Actis, M., Aghajani, T., Agnetta, G., Aguilar, J., Aharonian, F., Ajello, M., Akhperjanian, A., Alcubierre, M., Aleksic, J., et al., Mar. 2013. Introducing the CTA concept. *Astroparticle Physics* 43, 3–18.
- Aharonian, F., Akhperjanian, A. G., Bazer-Bachi, A. R., Beilicke, M., Benbow, W., Berge, D., Bernlöhr, K., Boisson, C., Bolz, O., Borrel, V., Braun, I., Breitling, F., Brown, A. M., Bühler, R., Büsching, I., Carrigan, S., Chadwick, P. M., Chounet, L.-M., Cornils, R., Costamante, L., Degrange, B., Dickinson, H. J., Djannati-Ataï, A., O’C. Drury, L., Dubus, G., Egberts, K., Emanoulopoulos, D., Espigat, P., Feinstein, F., Ferrero, E., Fiasson, A., Fontaine, G., Funk, S., Funk, S., Gallant, Y. A., Giebels, B., Glicenstein, J. F., Goret, P., Hadjichristidis, C., Hauser, D., Hauser, M., Heinzlmann, G., Henri, G., Hermann, G., Hinton, J. A., Hofmann, W., Holleran, M., Horns, D., Jacholkowska, A., de Jager, O. C., Khélifi, B., Komin, N., Konopelko, A., Kosack, K., Latham, I. J., Le Gallou, R., Lemièrre, A., Lemoine-Goumard, M., Lohse, T., Martin, J. M., Martineau-Huynh, O., Marcowith, A., Masterson, C., McComb, T. J. L., de Naurois, M., Nedbal, D., Nolan, S. J., Noutsos, A., Orford, K. J., Osborne, J. L., Ouchrif, M., Panter, M., Pelletier, G., Pita, S., Pühlhofer, G., Punch, M., Raubenheimer, B. C., Raue, M., Rayner, S. M., Reimer, A., Reimer, O., Ripken, J., Rob, L., Rolland, L., Rowell, G., Sahakian, V., Saugé, L., Schlenker, S., Schlickeiser, R., Schwanke, U., Sol, H., Spangler, D., Spanier, F., Steenkamp, R., Stegmann, C., Superina, G., Tavernet, J.-P., Terrier, R., Théoret, C. G., Tluczykont, M., van Eldik, C., Vasileiadis, G., Venter, C., Vincent, P., Völk, H. J., Wagner, S. J., Ward, M., Oct. 2006. Observations of the Crab nebula with HESS. *A&A*457, 899–915.
- Aleksic, J., Alvarez, E. A., Antonelli, L. A., Antoran, P., Asensio, M., Backes, M., Barrio, J. A., Bastieri, D., Becerra González, J., Bednarek, W., Berdyugin, A., Berger, K., Bernardini, E., Biland, A., Blanch, O., Bock, R. K., Boller, A., Bonnoli, G., Borla Tridon, D., Braun, I., Bretz, T., Cañellas, A., Carmona, E., Carosi, A., Colin, P., Colombo, E., Contreras, J. L., Cortina, J., Cossio, L., Covino, S., Dazzi, F., de Angelis, A., de Caneva, G., de Cea Del Pozo, E., de Lotto, B., Delgado Mendez, C., Diago Ortega, A., Doert, M., Domínguez, A., Dominis Prester, D., Dorner, D., Doro, M., Elsaesser, D., Ferenc, D., Fonseca, M. V., Font, L., Fruck, C., García López, R. J., Garczarczyk, M., Garrido, D., Giavitto, G., Godinović, N., Hadasch, D., Häfner, D., Herrero, A., Hildebrand, D., Höhne-Mönch, D., Hose, J., Hrupec, D., Huber, B., Jogler, T., Kellermann, H., Klepser, S., Krähenbühl, T., Krause, J., La Barbera, A., Lelas, D., Leonardo, E., Lindfors, E., Lombardi, S., López, M., López-Oramas, A., Lorenz, E., Makariev, M., Maneva, G., Mankuzhiyil, N., Mannheim, K., Maraschi, L., Mariotti, M., Martínez, M., Mazin, D., Meucci, M., Miranda, J. M., Mirzoyan, R., Miyamoto, H., Moldón, J., Moralejo, A., Munar-Adrover, P., Nieto, D., Nilsson, K., Orito, R., Oya, I., Paneque, D., Paoletti, R., Pardo, S., Paredes, J. M., Partini, S., Pasanen, M., Pauss, F.,

- Perez-Torres, M. A., Persic, M., Peruzzo, L., Pilia, M., Pochon, J., Prada, F., Prada Moroni, P. G., Prandini, E., Puljak, I., Reichardt, I., Reinthal, R., Rhode, W., Ribó, M., Rico, J., Rügamer, S., Saggion, A., Saito, K., Saito, T. Y., Salvati, M., Satalecka, K., Scalzotto, V., Scapin, V., Schultz, C., Schweizer, T., Shayduk, M., Shore, S. N., Sillanpää, A., Sitarek, J., Snidaric, I., Sobczynska, D., Spanier, F., Spiro, S., Stamatescu, V., Stamerra, A., Steinke, B., Storz, J., Strah, N., Surić, T., Takalo, L., Takami, H., Tavecchio, F., Temnikov, P., Terzić, T., Tesaro, D., Teshima, M., Tibolla, O., Torres, D. F., Treves, A., Uellenbeck, M., Vankov, H., Vogler, P., Wagner, R. M., Weitzel, Q., Zabalza, V., Zandanel, F., Zanin, R., Feb. 2012. Performance of the MAGIC stereo system obtained with Crab Nebula data. *Astroparticle Physics* 35, 435–448.
- Anderson, J., Byrum, K., Dawson, J., Drake, G., Haberichter, B., Horan, D., Krennrich, F., Kreps, A., Madhavan, A., Schroedter, M., Smith, A., Oct 2008. A new high-speed pattern recognition trigger for ground-based telescope arrays used in gamma ray astronomy. In: Nuclear Science Symposium Conference Record, 2008. NSS '08. IEEE. pp. 2773–2780.
- Berndlör, K., Oct. 2008. Simulation of imaging atmospheric Cherenkov telescopes with CORSIKA and sim_telarray. *Astroparticle Physics* 30, 149–158.
- Contreras, J. L., Satalecka, K., Berndlör, K., Boisson, C., Bregeon, J., Bulgarelli, A., de Cesare, G., de los Reyes, R., Fioretti, V., Kosack, K., Lavalley, C., Lyard, E., Marx, R., Rico, J., Sanguillot, M., Servillat, M., Walter, R., Ward, J. E., CTA consortium, A. Z. f. t., Aug. 2015. Data model issues in the Cherenkov Telescope Array project. ArXiv e-prints.
- Dwek, E., Krennrich, F., 2013. The extragalactic background light and the gamma-ray opacity of the universe. *Astroparticle Physics* 43, 112 – 133, seeing the High-Energy Universe with the Cherenkov Telescope Array - The Science Explored with the {CTA}.
URL <http://www.sciencedirect.com/science/article/pii/S0927650512001752>
- Fegan, D. J., Sep. 1997. TOPICAL REVIEW: γ /hadron separation at TeV energies. *Journal of Physics G Nuclear Physics* 23, 1013–1060.
- Funk, S., Hermann, G., Hinton, J., Berge, D., Berndlör, K., Hofmann, W., Nayman, P., Toussenel, F., Vincent, P., Nov. 2004. The trigger system of the H.E.S.S. telescope array. *Astroparticle Physics* 22, 285–296.
- Holder, J., Atkins, R. W., Badran, H. M., Blaylock, G., Bradbury, S. M., Buckley, J. H., Byrum, K. L., Carter-Lewis, D. A., Celik, O., Chow, Y. C. K., Cogan, P., Cui, W., Daniel, M. K., de la Calle Perez, I., Dowdall, C., Dowkontt, P., Duke, C., Falcone, A. D., Fegan, S. J., Finley, J. P., Fortin, P., Fortson, L. F., Gibbs, K., Gillanders, G., Glidewell, O. J., Grube, J., Gutierrez, K. J., Gyuk, G., Hall, J., Hanna, D., Hays, E., Horan, D., Hughes, S. B., Humensky, T. B., Imran, A., Jung, I., Kaaret, P., Kenny, G. E., Kieda, D., Kildea, J., Knapp, J., Krawczynski, H., Krennrich, F., Lang, M. J., LeBohec, S., Linton, E., Little, E. K., Maier, G., Manseri, H., Milovanovic, A., Moriarty, P., Mukherjee, R., Ogden, P. A., Ong, R. A., Petry, D., Perkins, J. S., Pizlo, F., Pohl, M., Quinn, J., Ragan, K., Reynolds, P. T., Roache, E. T., Rose, H. J., Schroedter, M., Sembroski, G. H., Sleege, G., Steele, D., Swordy, S. P., Syson, A., Toner, J. A., Valcarcel, L., Vassiliev, V. V., Wakely, S. P., Weekes, T. C., White, R. J., Williams, D. A., Wagner, R., Jul. 2006. The first VERITAS telescope. *Astroparticle Physics* 25, 391–401.
- Krennrich, F., Anderson, J., Buckley, J., Byrum, K., Dawson, J., Drake, G., Haberichter, W., Imran, A., Krawczynski, H., Kreps, A., Schroedter, M., Smith, A., 2008. A topological array trigger for agis, the advanced gamma ray imaging system. AIP Conference Proceedings 1085 (1), 894–897.
URL <http://scitation.aip.org/content/aip/proceeding/aipcp/10.1063/1.3076821>
- Krennrich, F., Lamb, R. C., Sep. 1995. Low energy γ -ray events in imaging Čerenkov telescope arrays. *Experimental Astronomy* 6, 285–292.
- López-Coto, R., Mazin, D., Paoletti, R., Blanch Bigas, O., Cortina, J., Apr. 2016. The Topo-trigger: a new concept of stereo trigger system for imaging atmospheric Cherenkov telescopes. *Journal of Instrumentation* 11, P04005.
- Moudden, Y., Venault, P., Barnacka, A., Calvet, D., Glicenstein, J.-F., Vivier, M., Aug. 2011. The Level 2 Trigger of the H.E.S.S. 28 Meter Cherenkov Telescope. *IEEE Transactions on Nuclear Science* 58, 1685–1691.
- Naumann, C. L., Tejedor, L. A., Martínez, G., Jun. 2013. COLIBRI: partial camera readout and sliding trigger for the Cherenkov Telescope Array CTA. *Journal of Instrumentation* 8, P06011.
- Otte, A. N., Biteau, J., Dickinson, H., Funk, S., Jogler, T., Johnson, C. A., Karn, P., Meagher, K., Naoya, H., Nguyen, T., Okumura, A., Santander, M., Sapozhnikov, L., Stier, A., Tajima, H., Tibaldo, L., Vandenbroucke, J., Wakely, S., Weinstein, A., Williams, D. A., CTA Consortium, f. t., Sep. 2015. Development of a SiPM Camera for a Schwarzschild-Couder Cherenkov Telescope for the Cherenkov Telescope Array. ArXiv e-prints.
- Paoletti, R., Cecchi, R., Corti, D., Dazzi, F., Mariotti, M., Pegna, R., Turini, N., Apr. 2007. The Trigger System of the MAGIC Telescope. *IEEE Transactions on Nuclear Science* 54, 404–409.
- Schroedter, M., Anderson, J., Byrum, K., Drake, G., Duke, C., Holder, J., Imran, A., Madhavan, A., Krennrich, F., Kreps, A., Smith, A., Aug. 2009. A Topological Trigger System for Imaging Atmospheric-Cherenkov Telescopes. ArXiv e-prints.
- Tibaldo, L., Vandenbroucke, J. A., Albert, A. M., Funk, S., Kawashima, T., Kraus, M., Okumura, A., Sapozhnikov, L., Tajima, H., Varner, G. S., Wu, T., Zink, A., CTA consortium, f. t., Aug. 2015. TARGET: toward a solution for the readout electronics of the Cherenkov Telescope Array. ArXiv e-prints.
- Vassiliev, V. V., Fegan, S. J., 2008. Schwarzschild-Couder two-mirror telescope for ground-based γ -ray astronomy. *International Cosmic Ray Conference* 3, 1445–1448.
- Weekes, T. C., Cawley, M. F., Fegan, D. J., Gibbs, K. G., Hillas, A. M., Kowk, P. W., Lamb, R. C., Lewis, D. A., Macomb, D., Porter, N. A., Reynolds, P. T., Vacanti, G., Jul. 1989. Observation of TeV gamma rays from the Crab nebula using the atmospheric Čerenkov imaging technique. *ApJ* 342, 379–395.
- Weinstein, A., 2008. The VERITAS Trigger System. *International Cosmic Ray Conference* 3, 1539–1542.
- Zitzer, B. f., Jul. 2013. The VERITAS Upgraded Telescope-Level Trigger Systems: Technical Details and Performance Characterization. ArXiv e-prints.